Corrigendum

Corrigendum: Computational methods for 2D materials: discovery, property characterization, and application design (2017 *J. Phys.: Condens. Matter* **29 473001**)

J T Paul[1]**, A K Singh**[2,3]**, Z Dong**[4]**, H L Zhuang**[5]**, B C Revard**[6]**, B Rijal**[1]**,
M Ashton**[1]**, A Linscheid**[7]**, M Blonsky**[6]**, D Gluhovic**[4]**, J Guo**[4]
and R G Hennig[1,8]

[1] Department of Materials Science and Engineering, University of Florida, Gainesville, FL 32611,
United States of America
[2] Lawrence Berkeley National Laboratory, Energy Technologies Area, Berkeley, CA 94720,
United States of America
[3] Joint Center for Artificial Photosynthesis, California Institute of Technology, Pasadena, CA, 91125,
United States of America
[4] Department of Electrical Engineering, University of Florida, Gainesville, FL 32611,
United States of America
[5] School for Engineering of Matter, Transport and Energy, Arizona State University, Tempe, AZ 85287,
United States of America
[6] Department of Materials Science and Engineering, Cornell University, Ithaca, NY 14850,
United States of America
[7] Department of Physics, University of Florida, Gainesville, FL 32611, United States of America

E-mail: rhennig@ufl.edu

CrossMark

ORCID iDs

A K Singh https://orcid.org/0000-0002-7212-6310
Z Dong https://orcid.org/0000-0003-2765-9764
H L Zhuang https://orcid.org/0000-0001-7276-7938
R G Hennig https://orcid.org/0000-0003-4933-7686

[8] Author to whom any correspondence should be addressed.

Topical Review

Computational methods for 2D materials: discovery, property characterization, and application design

J T Paul[1]**, A K Singh**[2,3]**, Z Dong**[4]**, H Zhuang**[5]**, B C Revard**[6]**, B Rijal**[1]**, M Ashton**[1]**, A Linscheid**[7]**, M Blonsky**[6]**, D Gluhovic**[4]**, J Guo**[4] **and R G Hennig**[1]

[1] Department of Materials Science and Engineering, University of Florida, Gainesville, Fl 32611, United States of America
[2] Energy Technologies Area, Lawrence Berkeley National Laboratory, Berkeley, CA 94720, United States of America
[3] Joint Center for Artificial Photosynthesis, California Institute of Technology, Pasadena, CA 91125, United States of America
[4] Department of Electrical Engineering, University of Florida, Gainesville, Fl 32611, United States of America
[5] School for Engineering of Matter, Transport and Energy, Arizona State University, Tempe, AZ 85287, United States of America
[6] Department of Materials Science and Engineering, Cornell University, Ithaca, NY 14850, United States of America
[7] Department of Physics, University of Florida, Gainesville, Fl 32611, United States of America

E-mail: rhennig@ufl.edu

Abstract
The discovery of two-dimensional (2D) materials comes at a time when computational methods are mature and can predict novel 2D materials, characterize their properties, and guide the design of 2D materials for applications. This article reviews the recent progress in computational approaches for 2D materials research. We discuss the computational techniques and provide an overview of the ongoing research in the field. We begin with an overview of known 2D materials, common computational methods, and available cyber infrastructures. We then move onto the discovery of novel 2D materials, discussing the stability criteria for 2D materials, computational methods for structure prediction, and interactions of monolayers with electrochemical and gaseous environments. Next, we describe the computational characterization of the 2D materials' electronic, optical, magnetic, and superconducting properties and the response of the properties under applied mechanical strain and electrical fields. From there, we move on to discuss the structure and properties of defects in 2D materials, and describe methods for 2D materials device simulations. We conclude by providing an outlook on the needs and challenges for future developments in the field of computational research for 2D materials.

Keywords: 2D materials, monolayers, density-functional theory, band structure, computational methods, phonons, magnetism

(Some figures may appear in colour only in the online journal)

1. Introduction

Since the discovery of graphene, [1] the field of two-dimensional (2D) materials and research on the discovery, characterization, and application of novel 2D materials has grown exponentially. This excitement was initially due to the extraction of a 2D crystal whose existence was ruled out by earlier harmonic approximation theories of Mermin and Wagner [2] but later proven to be stable due to coupling between bending and stretching modes [3, 4]. The remarkable properties of graphene, such as the presence of a Dirac cone, and thus high conductivity in the monolayer, further motivated the investigation of other potential 2D materials. The next several 2D materials to be discovered were hexagonal boron nitride (h-BN), with a wide band gap, [5, 6] MoS_2, which displays an indirect to direct band gap transition between the bulk and monolayer forms, [7] and other members of the 2D transition metal dichalcogenide (TMDC) class of materials with predominantly semiconducting nature and band gaps larger than their bulk counterparts [8].

More recently, III–V semiconductors, [9] metal oxides, [10, 11] MXenes, [12, 13] II–VI semiconductors, [14, 15] and many other compositionally diverse 2D materials [16–20] have been predicted and in some cases synthesized. While the first 2D materials—graphene and h-BN—are atomically thin, most 2D materials possess a finite thickness. They are still commonly categorized as 2D materials, and they typically possess significantly different properties than their bulk counterparts [7, 8, 13, 17, 21, 22].

2D materials can be difficult to synthesize due to their extremely thin nature, and the fact that they are not the thermodynamic ground state of a given materials system. Novel experimental techniques have been developed to synthesize and characterize 2D materials, both freestanding and supported on substrates. 2D monolayers can be obtained from certain layered bulk precursors by means of mechanical [23–26] or chemical [27] exfoliation. Deposition on a substrate is another popular method for creating 2D materials [28–30]. Predicting the structure and composition of a 2D material on a given substrate is the subject of intensive ongoing research [22, 31–34]. Computational approaches provide a valuable guide for experimental efforts toward the synthesis of 2D materials with specific structures and properties. Such approaches can discover novel monolayers, [9, 17, 21, 35, 36] identify suitable substrates for their synthesis and growth, characterize their properties, and predict their performance when used in devices.

So far close to one hundred 2D materials have been synthesized, several hundred more are predicted to be stable, and many more are likely awaiting discovery. The rapid growth of the family of 2D materials, with a broad range of properties suitable for many applications, presents an exciting opportunity for researchers to explore an entirely new class of materials. This opportunity has come at a time when mature computational methods provide the predictive capability to enable the computational discovery, characterization, and design of 2D materials as well as provide the needed input and guidance to experimental studies.

Several reviews have been written on the topic of 2D materials [37–39], on specific 2D materials, including graphene, [40–43] h-BN, [44] transition metal dichalcogenides, [8, 45] MXenes, [46] metal oxides, [47] and phosphorene, [48] and for van der Waals (vdW) heterostructures [49, 50]. These articles focus on experimental works and methods, but provide some discussion on computational methods. Review articles with a focus on computational methods have been written on the discovery and characterization of 2D materials, [32] the design of 2D materials for specific applications, such as photocatalysis, [51] and multiscale methods for graphene-based materials [52].

In this work, we review the state of modern computational methods available for studying 2D materials. In section 2, we generalize the structure classification of bulk materials to provide definitions that include the classification of two-dimensional materials structures. We then continue to provide a brief overview of density-functional theory approaches and cyber infrastructures for 2D materials in section 3, discuss the general criteria for thermodynamic stability and computational methods to assess the stability of 2D materials in section 4, and describe approaches for the discovery of novel 2D materials in section 5. We then consider computational methods to assess the environmental stability of 2D materials in section 6. We next move on to computational methods for the characterization of the various properties of 2D materials in sections 7–10. We continue by discussing defects and their role in 2D materials in section 11, and following a short foray into synthesis methods for monolayers and heterostructures in section 12 we describe modeling approaches for heterostructures devices in section 13. We conclude in section 14 by looking towards the future of 2D materials and discuss where novel computational tools and research is needed. The breadth of computational methods for 2D materials and the comprehensive coverage of this broad field in our review requires that we will refer the reader to the literature for some more in-depth discussions throughout this work.

2. Structure of 2D materials

2.1. 2D structure definition and classification

We begin by extending the classification of bulk materials' structures to 2D materials. We define a 2D material as a material with a finite thickness in one dimension and an essentially infinite extent in the other two dimensions. In practice, the thickness of 2D materials ranges up to about a nanometer, a scale below which the thickness strongly affects the materials' properties. The extent in the other dimension should be sufficiently large such that the edges should not affect the overall properties. Otherwise, the material should be classified as a one-dimensional material, e.g. a wire or ribbon, or as a zero-dimensional material, e.g. a nanoparticle, cluster, or molecule.

Similar to 3D materials, [55] we can further classify 2D materials into crystalline and amorphous materials. Crystalline 2D materials are 2D materials with long-range order in only two dimensions that leads to essentially discrete diffraction
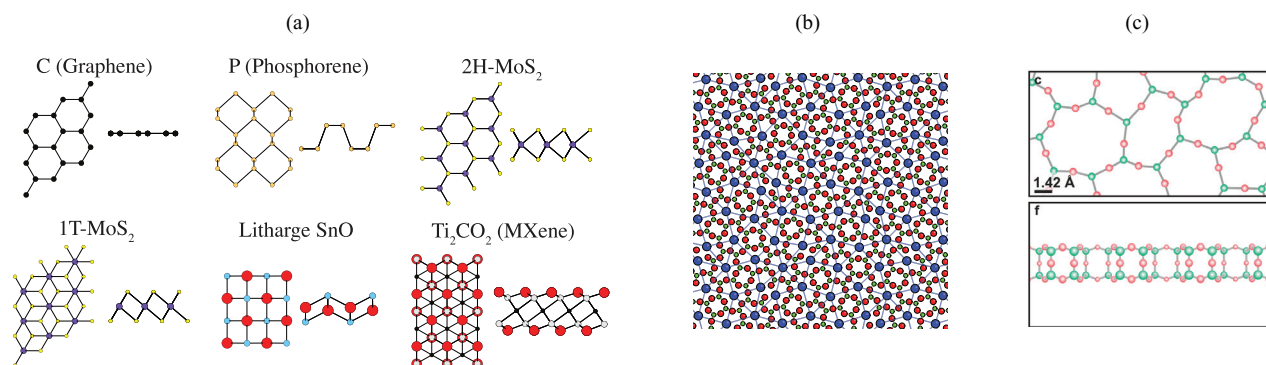
Figure 1. The three classes of 2D material structures. Structures of (a) well-known periodic crystalline 2D materials, (b) 2D quasicrystalline structure of $BaTiO_3$. (reprinted figure with permission from [53], Copyright 2016 by the American Physical Society) and (c) amorphous 2D structure of SiO_2. Reproduced from [54]. CC BY 4.0.

patterns, and a finite extent in the third dimension. The class of crystalline materials includes periodic crystals that exhibit translational symmetry and aperiodic crystals. Based on their point group symmetry, we further classify aperiodic crystals into incommensurate crystals and quasicrystals. Aperiodic crystals exhibit translational order but not translational symmetry; they display symmetries in their diffraction patterns, e.g. five or twelve-fold, [56] which are incompatible with periodic symmetry and, hence, not possible in periodic crystalline solids. Amorphous 2D materials lack long-range order and do not display discrete diffraction patterns.

2.2. Examples of 2D structures

Figure 1 shows examples of crystalline, quasicrystalline, and amorphous 2D materials. Most 2D materials, such as graphene, h-BN, and TMDCs belong to the family of periodic 2D crystals. The first quasicrystalline 2D material is $BaTiO_3$ grown on Pd, which exhibits a twelve-fold symmetry that is incompatible with translational symmetry [53, 57]. The first amorphous 2D material is SiO_2, the world's thinnest glass, with a bilayer structure of silica tetrahedra that form a continuous network of mostly 5, 6, and 7-membered rings [54, 58].

Several of the crystal structures shown in figure 1(a) correspond to single layers in naturally occurring vdW layered solids. This is true for many stable 2D materials. The vdW interlayer forces in layered solids are quite weak and responsible for only a small part of the material's overall Gibbs free energy [17, 59, 60]. As a result, the existence of a naturally occurring vdW layered solid often indicates the existence of a viable 2D crystal structure. This is why, as will be discussed in section 5.1, systematic searches for layered materials among bulk materials databases have been able to predict such a large number of stable 2D materials.

There are certain stable 2D materials, however, which have no naturally occurring layered bulk parent structure. The bi-tetrahedral crystal structure of 2D SiO_2, shown in figure 1(c), is one such example. The lowest energy crystal structures of these 'orphan' 2D materials are harder to predict, but computational methods exist to uncover them as well. We discuss these methods in some detail in sections 5.2–5.5.

2.3. Polymorphism in 2D materials

Some 2D materials can occur in different polymorphs that are either sufficiently close in energy to be experimentally observable, or stabilized through substrates or by doping. For these 2D materials, the structural difference between the polymorphs can significantly impact the properties of the compound [20, 61–69]. For example, 2D MoS_2 is most stable in the semiconducting $2H$ phase, but also displays a metallic $1T$ and a small band gap topological insulator $1T'$ polymorph [61, 62]. For 2D phosphorene, several polymorphs have been predicted, including blue phosphorene with an indirect band gap of 2 eV, which is energetically nearly degenerate with black phosphorene with a direct band gap of about 1 eV [20, 63, 64]. 2D antimonene exhibits two polymorphs, α and β, which are both dynamically stable and have significantly different band structures, though the α phase is lower in energy [65].

3. Computational methods and cyber infrastructure

3.1. Brief history of DFT

The properties of 2D materials are usually computed using the framework of density functional theory (DFT) [9, 17, 22, 35, 70, 71]. Even though the idea of describing quantum systems in terms of their density dates back to the Thomas–Fermi model [72, 73] and the Weizsäcker kinetic energy functional, [74] Hohenberg and Kohn were the first to show that the ground-state electronic density indeed determines all properties of an interacting many-body quantum, [75] thereby putting these ideas on a firm footing. While Hohenberg and Kohn established that knowledge of the ground state electron density in principle determines the ground state energy, they provided no direct way of calculating it. Kohn and Sham [76] proposed to construct an auxiliary non-interacting system with a single particle potential whose electron density agrees with that of the interacting system. The exact ground state energy is then formally written as a functional of the density, and since a single particle problem is a numerically tractable problem, given this single-particle Kohn–Sham potential, the energy can be calculated. Aside from the external potential, which determines the system, the Hartree potential contribution is

treated exactly. The remainder, originating from exchange and correlation (xc) contributions, has to be approximated.

3.2. Exchange-correlation functionals

Kohn–Sham in their work on the auxiliary system already proposed the local density approximation (LDA) for exchange and correlation, which replaces the xc potential locally at each point in the unit cell with the xc potential of the interacting electron gas with the same density [76]. The exchange part is calculated analytically; however, the correlation cannot, and LDA functionals[77–79] are usually based on parameterizations of quantum Monte Carlo calculations [80]. One of the most widely used LDA functionals is that of Perdew and Wang [79]. The LDA leads to good total energies for metals but is known to underestimate bond lengths [81].

More accurate functionals rely on similar ideas but also include additional information about the electron density, such as its gradients in the generalized gradient approximation (GGA), and additionally the curvature or kinetic energy density in meta-GGA functionals. Several flavors of GGAs exist, with two of the most widely used ones being the Perdew–Burke–Ernzerhof functional (PBE) [82] and the Becke-88 functional [83]. GGA type functionals usually further improve total energy predictions for solids and molecules and predict lattice parameters very accurately as compared to experiment. The outstanding accuracy and computational efficiency of these semi-local functionals makes DFT the standard method in computational materials science and chemistry, and condensed-matter theory.

3.3. Hybrid functionals for accurate band gaps

A common shortcoming of semi-local functionals is the underestimation of a possible band gap in the system. This effect is ultimately related to the derivative discontinuity of the exact exchange and correlation potential with respect to the particle number, which the LDA and GGA type approximations are missing [84]. The PBE0 [85] and Heyd–Scuseria–Ernzerhof (HSE) [86] functionals include, e.g. 25% of the exact exchange contribution, which improves the agreement of the Kohn–Sham band gap with experiment, [84] as well as the defect formation energies [87, 88] and phase transition pressures for metal-insulator transitions [89]. Because they contain both DFT and Hartree–Fock contributions these functionals are referred to as hybrid functionals. Note that the explicit dependence of the functional, now not only on the density but also on the Kohn–Sham wavefunctions, leads to a significant increase in computational cost. Meta-GGAs also improve band gaps to some extent while being in general less expensive [84]. Both in computational cost and accuracy, they range in between GGAs and the hybrid functionals.

3.4. DFT + U method

DFT with semi-local and hybrid exchange-correlation functionals accurately describes the structural and electronic properties of bulk materials. However, in some materials, strong electronic correlation present additional challenges and

require special treatment. In a broad sense, correlations are effects that cannot be incorporated into an effective non-interacting system which naturally makes them hard to describe in a Kohn–Sham single-particle system. Especially for strongly localized states with a small overlap between neighboring lattice sites, the correlation energy can dominate and behave very differently from the homogeneous electron gas that provides the starting point for the functional construction. It is possible to correct for the shortcomings of these functionals by selecting these localized states and describing them with an independent Hubbard model of electrons interacting with an effective screened Coulomb interaction U. In practice, this Hubbard interaction, U, in this DFT + U treatment is an adjustable parameter with common values for various materials classes [90–92].

3.5. Many-body methods

The most accurate method to compute band gaps is based on the Dyson equation for the single particle Green's function, G. Hedin reformulated the exact solution of the Schrödinger equation in terms of five coupled integral equations and suggested an approximation that neglects the screening of the electron vertex function [93]. The result is a system of equations where the screening of the Coulomb interaction, W, is treated within the random phase approximation (RPA), which then enters the equation for the Green's function via the self-energy $G \cdot W$, hence the name GW approximation.

In practice, DFT is used to obtain a starting system, and different levels of self-consistency are imposed to arrive at a final solution. The G_0W_0 approximation computes the screening in the Kohn–Sham system, W_0, and the self-energy is constructed with the Kohn–Sham Green's function, G_0, to update the Kohn–Sham energies. The partially self-consistent GW_0 approximation imposes self-consistency at the level of the Green's function but keeps the screening fixed. Finally, the fully self-consistent GW approximation treats both the Green's function and the screening it provides self-consistently [94]. It is observed that the GW_0 matches the experimental data well and that the significantly more computationally expensive fully self-consistent GW method provides similar results.

While GW-type methods yield accurate single electron excitations, computing neutral two particle interactions such as electron-hole pair or exciton interactions requires a more accurate calculation of the polarizability at the level of the Bethe–Salpeter equations (BSE) [95]. Interactions of this kind are important in the calculation of optical absorption spectra, but are numerically very expensive. Alternatively, time dependent DFT can be applied to compute optical spectra of solids, which is numerically much more efficient while usually less accurate [96–98].

3.6. Van der Waals interactions

Another intrinsically non-local effect that semi-local DFT functionals fail to describe are vdW interactions. Especially for layered materials, the neglect of this effect can lead to significant underestimation of the bonding energy and interlayer

distance. Common methods to account for this effect range from empirical corrections, [99, 100] to non-local exchange correlation functionals, [101, 102] to full many-body treatment of vdW interactions [103, 104]. Comparison with more accurate and computationally demanding RPA calculations show that these non-local functionals and the many-body treatment of vdW interactions reproduce relative trends in exfoliation energy and predict the interlayer interactions within 30% of the RPA [17, 105, 106]. The vdW interactions are of particular importance for 2D materials, where energies are to be compared to bulk references. If the bulk material is layered, semi-local functionals will underestimate the binding energy. As discussed in the previous section, layered bulk materials provide an important set of candidate materials for exfoliation of 2D materials.

3.7. Software packages

DFT methods have mostly been developed on and for bulk 3D materials. However, functionals show very accurate performance also in reduced dimensions [107] for many materials systems. Similarly, most Kohn–Sham DFT software packages are designed for 3D systems and employ periodic boundary conditions. The standard method for calculations of 2D materials is to approximate the 2D material by a slab embedded in a 3D simulation cell. Periodic images of the slab must be separated by a sufficiently large region of vacuum. Especially for layers which lack inversion symmetry or exhibits an electric dipole moment, this setup has to be treated with care since periodic replicas will be present in the third dimension which can lead to spurious interactions if the vacuum is not sufficiently large. Widely used software packages that can perform DFT calculations for 2D materials include VASP [108–110], Quantum Espresso, [111] ABINIT, [112] and CASTEP [113].

3.8. High-throughput frameworks

Bahn and Jacobsen were among the first to realize the potential of a highly automatic framework to systematically setup, run, and analyze DFT calculations when they developed the atomic simulation environment (ASE) [114]. The package prepares, runs, manipulates, and analyzes results from a wide array of simulation packages.

A decade later, python materials genomics (Pymatgen) was developed [115]. This tool manipulates input and analyzes output files of various DFT software packages and interfaces with the materials project database of materials. Recently, the package MPInterfaces has been developed to aid the study of nanoparticles and interfaces [116]. In addition, it provides a framework for high throughput submission and screening of simulations for DFT software packages. These tools make the acquisition and analysis of material data far more efficient, increasing the speed of computational research.

3.9. Materials databases

It has become increasingly common to make calculated materials data available through online databases. Databases which host data specifically for 2D materials include the computational materials repository [117], the Midwest Nano Infrastructure Corridor 2D Database [118], and the MaterialsWeb database [17]. In order to facilitate large scale analysis, some of these databases provide high-throughput application programming interfaces (APIs) to their data. MaterialsWeb, for example, uses the Materials API developed for the Materials Project and Pymatgen. With this API, users can systematically access the DFT data on the Materials Project or MaterialsWeb databases using programs written in python.

4. Thermodynamic stability

Materials are stable when they are in thermodynamic equilibrium. The second law of thermodynamics commands that for a material to be in equilibrium at constant pressure, p, and temperature, T, its Gibbs free energy must be a minimum. The Gibbs free energy, $G(p, T) = E + pV − TS$, has three contributions: the internal energy, E, the volume, V, and the entropy, S. For condensed phases, the pV contribution is usually negligible. The entropy contribution, TS, becomes increasingly important at higher temperatures. For solid materials, there are three main contributions to entropy: (i) the vibrational entropy due to phonons, (ii) the configurational entropy due to site disorder in alloys and point defects, and (iii) the electronic entropy due to excitations of the electrons across the Fermi level.

DFT-based methods can calculate the various contributions to the Gibbs free energy of a material. DFT is a ground state method and directly computes the internal energy, E, and the volume, V, given an external pressure, p. The contributions to the entropy are commonly calculated using separate methods.

(i) The vibrational entropy is determined by integrating the phonon spectrum for crystalline materials. The phonons can be accurately computed with DFT using either a finite displacement method [119] or using density functional perturbation theory (see [120] for a review). As non-interacting bosonic particles, the phonon contribution to the entropy is then easily computed according to the Bose-Einstein statistic. The Python code Phonopy [121] assists in setting up and analyzing these calculations.

(ii) The configurational entropy can be obtained from Monte Carlo calculations, which require the energy of site disorder and defect formation. DFT can in principle provide these energies. In practice, the vast number of possible configurations makes it unfeasible to directly determine all the energies using DFT, and surrogate models such as cluster expansions fit to DFT are used instead. Several software tools, such as ATAT [122, 123] and UNCLE, [124] can set up and submit the required DFT calculations, optimize the cluster expansion, and perform the Monte Carlo simulations to obtain the configurational entropy.

(iii) For the electronic contribution to the entropy at low to moderate temperatures where crystalline solids exist, it is

a reasonable approximation to use the zero temperature band structure and populate it according to the Fermi–Dirac statistic.

The vibrational and configurational entropy contributions of a material are bound from above by the Dulong-Petit law at $3/2kT$ per atom. The electronic entropy is negligible in semiconductors and insulators but can be significant in metals with a high electronic density of states at the Fermi level. Since it is the differences in the Gibbs free energy of materials that determines the thermodynamic stability, part of the entropy of materials cancels. For materials with similar Debye temperatures, site disorder, and band gaps or electronic density of states at the Fermi level, most of the entropy cancels and it is therefore a good approximation to neglect the entropy contribution to the Gibbs free energy [125, 126].

2D materials are not in thermodynamic equilibrium, and hence are inherently metastable since the stacking of monolayers always lowers the energy due to vdW attraction between the layers. Hence, when a 2D material is colloquially referred to as stable, it is understood that the monolayer is in fact thermodynamically metastable. For the synthesis, growth, and application of 2D materials, it is required that the 2D materials be sufficiently stable such that any processes that drive the transformation or decomposition of the 2D material are kinetically slow. For the computational study of the stability of 2D materials, we need to identify suitable criteria for sufficient stability. We will discuss the two complementary criteria of hull distance and surface energy in the following sections 4.1 and 4.2, respectively.

4.1. Hull distance

Early work on 2D materials presented negative enthalpies of formation as an indicator of thermodynamic stability in predicted 2D materials. However, since the enthalpy of formation is the energy difference between a material and its pure elemental constituents, it is a necessary but insufficient piece of evidence for materials stability. For a material to be thermodynamically stable, it must have a negative enthalpy of formation not only with respect to the pure constituents but relative to all possible competing phases.

Mathematically, the ground state phases for a multi-component materials system are those that lie on the convex hull of the Gibbs free energy as a function of composition, sometimes also referred to as the thermodynamic hull. Figure 2 illustrates the convex hull for the Fe–Cl system. Any phase not on the hull is thermodynamically unstable and can lower its energy by decomposing into one or more phases that do lie on the hull. Therefore, when evaluating the stability of a 2D material, the relevant thermodynamic measure is its distance above the convex hull of the ground state (bulk) phases.

A review of already existing 2D materials reveals that only those with hull distances <200 meV/atom were synthesized as free-standing monolayers [22, 51]. In light of this finding, we recommend using a threshold of 200 meV/atom for the hull distances of potential 2D materials as an upper bound on sufficient thermodynamic stability for the synthesis and growth of free-standing monolayers.
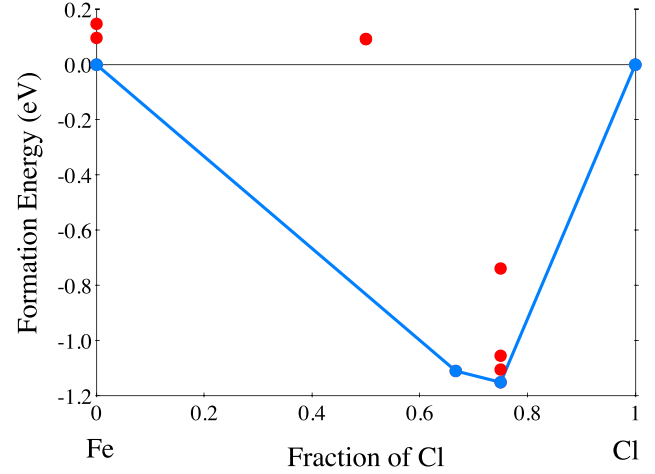

Figure 2. The phase diagram for the Fe–Cl system, derived from data at MaterialsProject.org [127–129]. The most stable phases are represented by blue circles, and the thermodynamic/convex hull is outlined in blue. Compounds above the hull are represented by red circles.

We note that the hull distance should not be confused with the exfoliation energy, which is the energy needed to exfoliate a monolayer from a layered bulk material. For 2D materials that correspond to monolayers exfoliated from a ground state layered bulk material, the hull distance and exfoliation energy are indeed the same. However, some layered bulk compounds are not thermodynamic ground states and several 2D materials lack any layered bulk structure from which they can be exfoliated. In the former case, the hull distance is in fact larger than the exfoliation energy and the exfoliation energy may overestimate the stability of the monolayer. In the latter case, no exfoliation energy exists. For thermodynamic reasons and consistency, we recommend the hull distance as the criterion for thermodynamic stability, and not the exfoliation energy nor the enthalpy of formation.

4.2. Surface energy

The surface energy, γ, provides an alternative measure of the thermodynamic stability of a 2D material, [22]

$$\gamma = \frac{N_{2D}}{2A} \Delta E_f, \qquad (1)$$

where ΔE_f is the formation energy relative to the bulk ground state(s), i.e. the hull distance, N_{2D} is the number of atoms in the cell of the 2D structure, and A is the in-plane area of the 2D material. The surface energy can be especially useful for evaluating the stability of 2D materials whose structures differ from those of their bulk counterparts. Also, in contrast to the distance from the convex hull, the surface energy is not as strongly affected by the number of layers in multilayer 2D materials, whereas the distance from the convex hull approaches that of the layered bulk compound [22]. Hence, the surface energy criteria for the stability of 2D materials may be advantageous for computational methods predicting novel 2D materials as will be discussed in section 5.
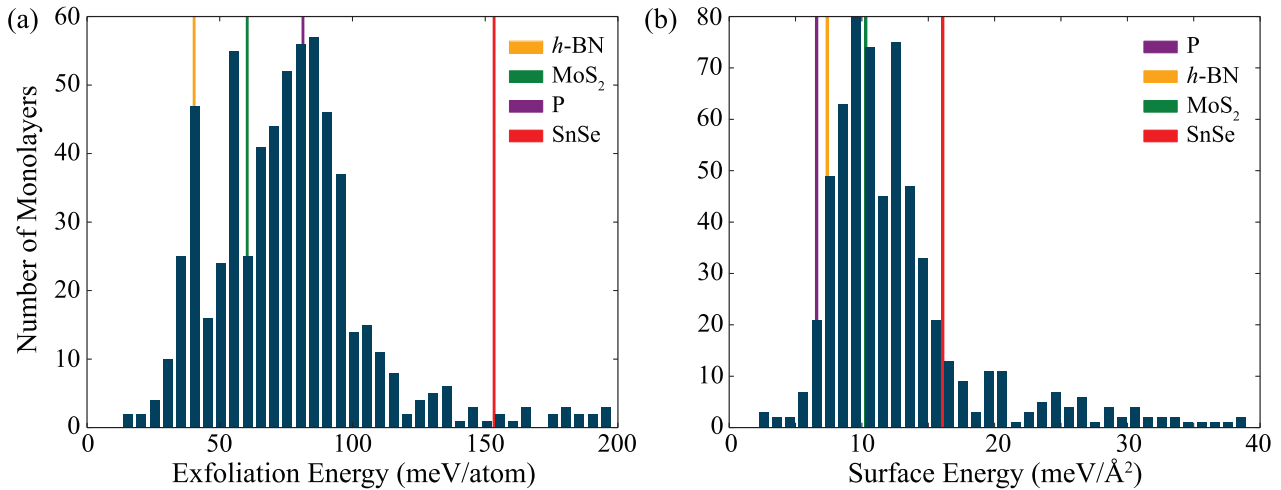
Figure 3. Histograms of (a) the hull distance and (b) surface energy criteria for evaluating the thermodynamic stability of 2D materials. The orange, green, purple, and red lines represent the energies of the monolayers *h*-BN, [105] MoS$_2$, [105] phosphorene, [130] and SnSe, [131] respectively, which have all been synthesized as free-standing layers.

4.3. Difference between standards

We compare the two stability criteria—hull distance and surface energy—using the MaterialsWeb database of over 600 2D materials [17, 132]. Note that most of the over 600 compounds in MaterialsWeb are exfoliated from ground state layered materials and a few from layered bulk materials with hull distances of up to 50 meV/atom. Hence, their exfoliation energy equals or is very similar to their hull distance.

Figure 3 shows the histograms for the two criteria and compares the criteria with the values for common 2D materials, *h*-BN, MoS$_2$, phosphorene, and SnSe. Although phosphorene and *h*-BN have significantly different exfoliation energies, their surface energies are very similar. SnSe, the most unstable 2D material that has been synthesized as a freestanding layer, [133] has the highest energy in both standards [131].

Figure 4 compares the two criteria across the over 600 2D materials of the MaterialsWeb database [17, 132]. Applying the exfoliation and surface energy of SnSe as the threshold for defining stability, we find that the surface energy criterion is stricter, resulting in approximately 10% fewer structures than the exfoliation energy threshold. However, the surface energy threshold also captures several monolayers, about 1%, that do not pass the exfoliation energy cutoff. In conclusion, both criteria are empirical and provide insight for evaluating monolayer stability.

4.4. Dynamic stability

Metastable materials, such as 2D materials, can exhibit another type of instability that originates from a lack of restoring forces when the structure is perturbed. Such instabilities are reflected in the phonon spectra of materials, where imaginary modes indicate unstable perturbations, which can lead to reconstructive or martensitic phase transformations. A classical example is the low-temperature instability of the bcc phase of Ti, which leads to martensitic phase transformations to either an hcp or ω phase [134–136].

When considering the stability of 2D materials, it is important to include the dynamic instability to identify possible reconstructions to lower-energy 2D structures. Empirically, 2D materials with larger exfoliation energy or convex hull distances are more likely to exhibit unstable modes since the energy of the structure is bound from below by the energy of the bulk phase. Figure 5 illustrates a dynamic instability in one of the polymorphs of 2D MoS$_2$. The imaginary modes in the higher energy 1T phase indicate a reconstruction of the structure and the formation of a charge-density wave at low temperatures.

DFT methods can compute the phonon spectrum of a material using either a finite displacement method [119] or density functional perturbation theory [120]. The unstable modes indicate the structural distortions that lead to the reconstructed structure. Creating appropriate supercells of unstable structures and perturbing the atom positions using the eigenvectors of the imaginary modes, followed by structural relaxations, can provide candidate structures for low-temperature reconstruction.

It is important to note that structures that display unstable phonon modes at zero temperature, as determined by DFT simulations, may still be thermodynamically stable at elevated temperatures. The calculation of the Gibbs free energy of such phases is, however, exacerbated by the unstable phonon modes and requires sampling methods such as thermodynamic integration [137] or self-consistent phonons [136, 138].

5. 2D materials discovery

The first step in successfully synthesizing novel 2D materials is identifying 2D structures that are thermodynamically metastable, as discussed in section 4. Several approaches to predicting 2D structures have been reported in the literature, and they may be broadly categorized into two classes. The first class includes methods that rely on the structures of already known materials, whether 2D or bulk, to identify candidate
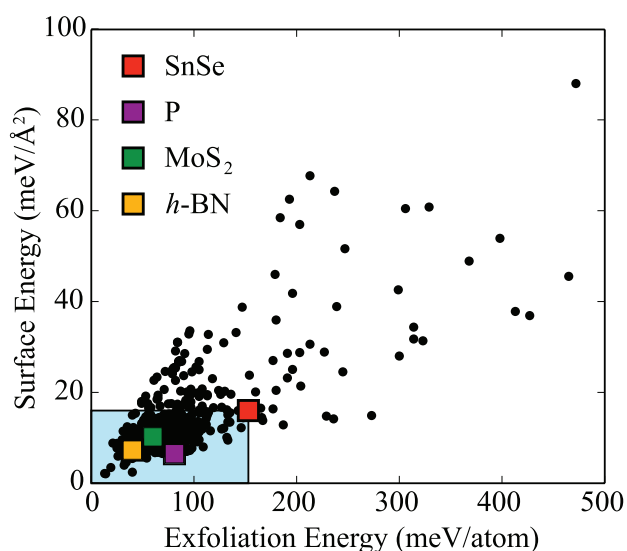
Figure 4. Comparison of the stability criteria for 2D materials—exfoliation energy versus surface energy for each of the 2D materials in the MaterialsWeb database discovered by Ashton *et al*. The orange, green, purple, and red squares represent the experimentally synthesized free-standing monolayers *h*-BN, [105] MoS$_2$, [105] phosphorene, [130] and SnSe [131] respectively. The shaded region shows the energy ranges containing monolayers that are considered the most feasible to synthesize as free-standing monolayers.

2D structures. Detailed descriptions of these approaches can be found in sections 5.1 and 5.4.

The second class of methods are algorithms that treat structure prediction as a global optimization problem. These optimization algorithms do not necessarily require knowledge of existing 2D or bulk crystal structures, and are therefore capable of performing unbiased searches for low-energy structures. However, global optimization algorithms generally require hundreds or thousands of objective function evaluations to achieve convergence. If DFT is used to relax candidate structures and compute their total energies, the computational cost of these structure searches can be considerable. Two such algorithms for structure prediction are described in sections 5.2 and 5.3.

5.1. Data mining

Graphene was originally obtained by mechanical exfoliation of graphite. This exfoliation is possible because graphite is composed of several stacked graphene layers, held together by weak vdW forces. There are many other vdW layered solids like graphite. As a result, efforts have been made to identify other layered bulk materials from which single layers could be isolated to form feasible 2D materials.

During these searches, databases of bulk crystal structures are screened to identify materials with layered features. To find new transition metal dichalcognide 2D materials, Ding *et al* considered materials that are chemically similar to MoS$_2$, which is known to form a layered vdW structure [71]. The bulk structures of these chemically similar compounds were identified in a database and found to display layered features, leading to several promising candidate 2D materials.

A more thorough search of crystal structure databases was performed later by Lebègue *et al* [21] They screened the inorganic crystal structure database (ICSD) [139] for materials with vdW bonded layers. They used the following criteria to determine whether a material was layered: packing fraction between 0.15 and 0.5, gaps along the *c* lattice vector between crystallographic planes greater than 2.4 Å, and absence of covalent bonds spanning these gaps. In addition, only structures yielding high symmetry square or hexagonal monolayers were considered. This filter was applied to all the structures in the ICSD to identify 92 single layer compounds.

Ashton *et al* recently developed another algorithm to identify layered structures [17]. This algorithm identifies networks of bonded atoms within the unit cell based on overlapping atomic radii. A $2 \times 2 \times 2$ supercell is then created, and the atoms are again grouped into bonded networks.

By comparing the number of atoms in the bonded network before and after forming the supercell, the dimensionality of the network can be determined. 2D layers display periodicity in only two dimensions, so if the the cell is doubled in each dimension, the network size in a layered structure will increase by a factor of four, while in a conventional bulk structure it will increase by a factor of eight.

This algorithm correctly identifies several unusual layered materials, shown in figure 6, such as layered crystals in which the gap between adjacent layers is undulated instead of planar. In addition, this algorithm does not rely on a particular crystallographic representation of layered structures (e.g. layers oriented normal to the *c* lattice vector) to be successful, can identify very thick layers, and discerns between 2D layered materials and those composed of 1D chains or 0D molecules. Over 800 layered materials with reasonable thermodynamic stability were identified by applying this algorithm to the structures in the Materials Project database. Monolayers from these materials can be found in the 2D materials database at materialsweb.org.

5.2. Genetic algorithms

In recent years, genetic algorithms have proven to be a useful approach to solving the global optimization problem. Genetic algorithms are inspired by the idea of biological evolution, as they evolve a population of candidate solutions over time. In the course of the algorithm, each structure is assigned a fitness. This is a measure of how low a structure's formation energy is relative to the other structures in the population. Structures with higher fitnesses are preferentially selected to create offspring, who are then evaluated and added to the population.

Offspring structures are primarily generated with a mating operator, which essentially slices a chunk from each of two parent structures and combines them together to form an offspring structure, as illustrated in figure 7. The mating operator is successful because it passes local structural traits from parents to offspring, and formation energy is largely a function of local structure. Over time, this causes structural traits correlated with low formation energy to propagate in the population, and traits causing high energy to die out.
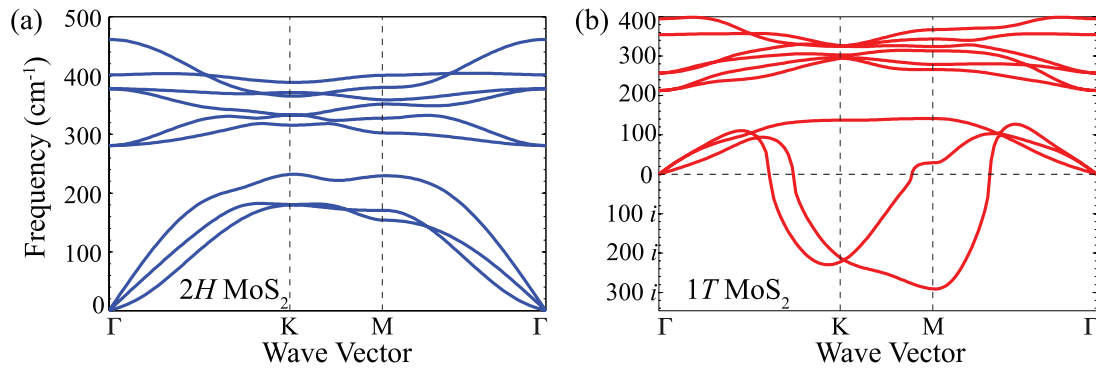
Figure 5. Phonon spectra of two polymorphs of 2D MoS$_2$: (a) the 2H structure and (b) the 1T. The presence of imaginary modes indicates that the 1T structure is not dynamically stable [62].

At least two modifications are usually required in order to apply genetic algorithms to search for 2D structures. The first involves constraining the search to the 2D regime, which is usually accomplished by enforcing a constraint on the thickness of the 2D structures considered by the algorithm. The second modification is needed because most codes for computing a structure's total energy assume periodicity in all three dimensions. Therefore, vertical vacuum padding must be added to 2D structures before their energies are computed to prevent them from interacting with their periodic images. It should be noted that the first modification can prevent the discovery of some monolayers if the thickness of that monolayer is greater than the imposed restriction.

Unlike some other methods for crystal structure prediction, genetic algorithms are not necessarily limited to searching spaces of fixed dimensionality. This is important because the number of atoms in the lowest energy structure is not usually known *a priori*, and even the compositions of the thermodynamic ground states cannot necessarily be assumed.

The key to a successful genetic algorithm optimization is maintaining diversity in the population. Deep local minima in the energy landscape have the chance to trap the algorithm and imply the global minimum has been reached. Thus, most algorithms have ways to perturb a population so that local minima can be escaped. These methods include swapping positions of atoms in unit cells, increasing/decreasing the lattice vector magnitudes, translating atoms in the unit cell, and adding randomly generated structures to the population.

Several authors have applied genetic algorithms to search for 2D structures of boron, [67, 140–142] carbon, [143] C$_n$O compounds, [144] InP and the C–Si and Sn–S 2D phase diagrams, [22] and group IV dioxides [70]. Publicly available codes that implement genetic algorithms for 2D crystal structure prediction include USPEX, [145] EVO, [140] and GASP [146]. A more in depth review of the genetic algorithm method has been conducted by Revard *et al* [147].

5.3. Particle swarm optimization

Particle swarm optimization (PSO) is another heuristic approach that has been successfully applied to predict 2D crystal structures. The algorithm starts with a group (swarm) of randomly generated structures (particles) and
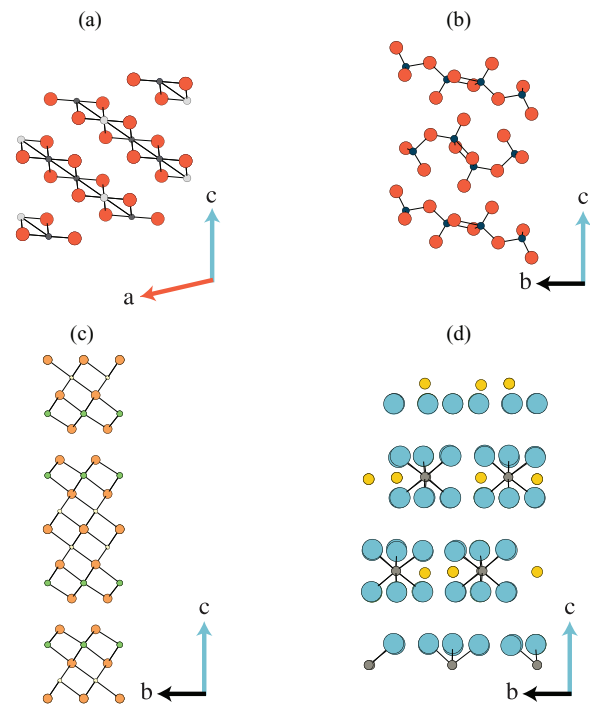

Figure 6. Example of structures that the topological scaling algorithm can find. This algorithm improves database searching by finding structures regardless of the gap direction (a), if the layers are intercalated (b), if the layers are very thick (c), and molecular structures that appear layered (d). Reprinted figure with permission from [17], Copyright 2017 by the American Physical Society.

then moves the particles in the swarm through the solution space. Specifically, a particle is shifted by a vector that is the weighted sum of three components: the particle's previous shift, the difference between the particle's current position and the best position previously seen by the particle, and the difference between the particle's current position and best position seen by the entire swarm of particles, where the weights on the latter two terms are drawn from a uniform distribution. Once a structure has been shifted, its energy is recomputed. In this way, the swarm of particles gradually converges toward the global minimum of the potential energy surface.

A PSO algorithm for 3D crystal structure prediction [148] was initially modified to search for completely planar
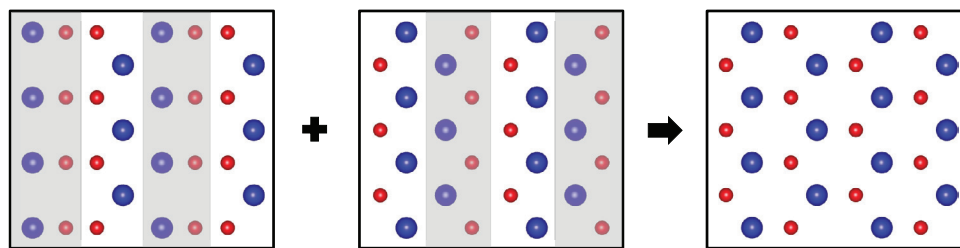
Figure 7. Illustration of the mating operator [22]. Sections are sliced from each parent structure, shown on the left, and combined to form an offspring structure. Supercells are shown for clarity. Reprinted figure with permission from [22], Copyright 2016 by the American Physical Society.

structures [149]. The algorithm was later modified further to search for 2D structures with non-zero thicknesses [150, 151]. Note that the modifications needed to enable 2D structure searches are essentially the same as those made to genetic algorithms: a constraint on the thickness of the 2D structures and the addition of vertical vacuum padding.

The modified PSO algorithm has been applied to several 2D systems containing boron and carbon [144, 149, 152–155]. However, most the these searches were restricted to completely planar structures, and the formation energies of the predicted 2D materials relative to the competing bulk phase(s) were not reported. As a result, one should determine their hull distance or surface energy before pursuing further research on these materials.

5.4. Chemical substitution

Chemical substitution is perhaps the most straightforward way to find novel 2D materials. The method entails taking known 2D structures, discovered from the previously described methods, and substituting different species at the atomic sites. This approach is simple and computationally inexpensive, making it a good first step to identify promising structures in a 2D system. It should be noted that chemical substitution does not usually lead to new structures (unless significant changes occur during structural relaxation), but rather to new site decorations of known lattices. As the collection of known 2D structures grows, this method becomes increasingly useful.

There are several methods to increase the accuracy of chemical substitution searches. First, one can use chemical intuition in order to decide what structures and elements to use in the substitution. If the elements substituted into a structure are likely to exist in uncommon oxidation states, they can often be screened out. Second, one can increase the number of structures used in the substitution for a given set of elements. Using 2D material databases, one can obtain a list of of structural templates based on known structures for a given ratio of elements. This allows for more certainty that the lowest energy structure has been discovered. Third, one can simulate supercells of a given structure rather than a single unit cell. While this increases the computational cost, using supercells enables the study of structural distortions and different magnetic configurations, which are not accessible with a single unit cell and may lower the system's energy.
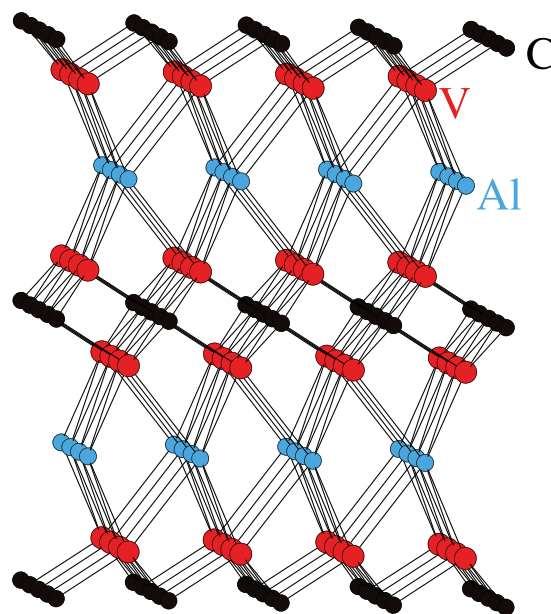

Figure 8. The V_2AlC MAX phase. The Al atoms can be etched away with an appropriate acid, leaving behind V_2C monolayers. The surfaces of these monolayers can then be passivated to obtain stable 2D materials. Reprinted figure with permission from [157], Copyright 2016 by the American Physical Society.

Şahin *et al* used this method to discover group IV and group III–V binary monolayers [9]. 2D transition metal dichalcogenides and dioxides with the 1 *T* and 2 *H* structures have also been identified with chemical substitution, [156] as well as group III–V single layer materials with a tetragonal structure [35].

5.5. Etching

Bulk materials databases can also be screened for materials that can be chemically etched to form 2D materials. This can be done by looking for bulk structures with repeating layers composed of galvanically active elements (e.g. Al) that can be dissolved by an acid. The details of a typical etching reaction are discussed in greater detail in section 12, but one can approach discovering these precursors from a computational perspective. By taking a known precursor phase and replacing some of its elements, one can sometimes discover novel bulk phases with the potential to yield novel 2D materials after selected layers of the crystal are dissolved.
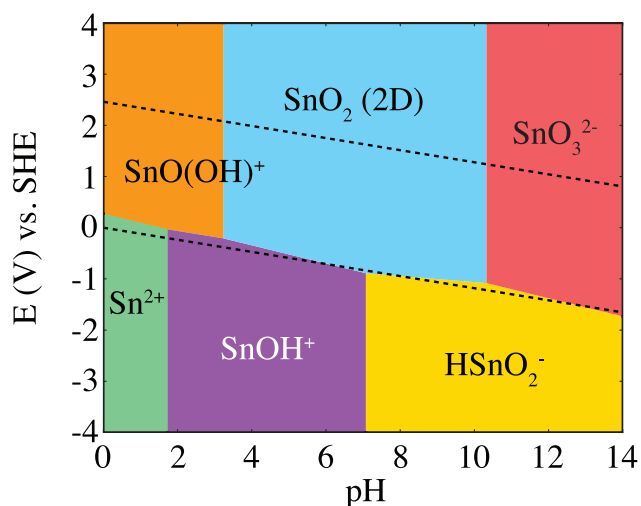
Figure 9. Pourbaix diagram for 2D SnO₂. The region between the dashed black lines represent the range of stability for H₂O. The light blue region is the range of pH and applied voltage in which SnO₂ is most stable. Derived from www.materialsweb.org [17].

One example of such a precursor phase is the MAX phase structure, shown in figure 8. HF can be used to selectively etch layers from these materials, leaving behind transition metal carbide/nitride monolayers known as MXenes. The majority of successful etchings have had Al as the dissolved layer [27, 46, 157–162]. The newly exposed transition metal surfaces can then be passivated with anions such as oxygen [13].

Obtaining insight into an etching process from a computational framework is challenging, and requires an accurate understanding of the relevant competing phases for the original bulk material, as well as for the desired 2D material, as a function of pH and choice of acid. A possible route to obtain this information is briefly described in the next section.

6. Environmental interactions

6.1. Stability in water

A 2D material's stability in an aqueous environment is quite different from its dry stability. The most straightforward reaction pathway for a 2D material to decompose in water generally involves the formation of ions and molecules in solution that would not form in air. Consequently, understanding a 2D material's stability in water requires considering these ions and molecules as competing phases when constructing its aqueous phase diagram.

To construct these phase diagrams computationally, it is expedient to use experimentally obtained formation energies of solvated ions and molecules that are difficult to calculate accurately in DFT. These experimental formation energies can be used in the same framework as the DFT-calculated formation energy of a 2D material after they are shifted based on the difference in experimental and DFT formation energies of a known reference material [163].

The free energy of each species in an aqueous environment is a function of concentration, pH, and applied potential in the solution, according to

$$G_i(c_i, pH, \phi) = G_i^0 + 0.0591 \log c_i - n_O \mu_{H_2O}$$
$$+ pH(n_H - 2n_O)$$
$$+ \phi(-n_H + 2n_O + q_i) \quad (2)$$

where c_i is the concentration, n_O and n_H are the respective numbers of oxygen and hydrogen atoms in the species, μ_{H_2O} is set to the formation energy of water of -2.46 eV, ϕ is the electric potential, and q_i is the species' charge. The variable nature of G_i enables the construction of Pourbaix diagrams, which plot a material system's stable phases as a function of pH and voltage. Therefore, these diagrams show what values of pH and voltage (if any) one can expect a given 2D material to remain stable and not dissolve.

As an example, the Pourbaix diagram generated for 2D SnO₂, where all ionic concentrations are set to 10^{-3} M, is provided in figure 9. SnO₂ has a large region of stability, indicating this material is likely to remain undissolved in water under normal conditions.

6.2. Sensitivity of properties to gaseous molecules

2D materials, when used in applications, are not isolated in vacuum. Thus, finding the impact of gaseous molecules on 2D materials is an ongoing area of research. The majority of research has been on graphene and TMDCs, especially MoS₂, and so the following section focuses on these classes of monolayers.

Determining adsorption energies of molecules on 2D materials is not unlike the process for bulk material surfaces, and requires the careful selection of adsorption sites and orientations of the gaseous molecules.

One also needs to decide what environment to calculate the adsorption energy in. Adsorption in vacuum is often a sensible choice and is the default in most DFT codes. To investigate adsorption in an aqueous environment, it is necessary to include a solvent either implicitly [164] or explicitly by adding the solvent molecules in the DFT calculation. If the adsorbate is charged, such as OH⁻ or H⁺, then explicit solvation is required.

6.2.1. Graphene.
The primary motive for investigating interaction between graphene and gaseous molecules has been for sensor detection. This detection usually relies on measuring any changes to graphene's conductivity upon the introduction of adsorbates [165–168].

There are three primary sites of adsorption, as shown in figure 10: on top of a carbon atom (T), between two carbon atoms (B), or in the center of the hexagon ring (C). For atoms and simple molecules, there are only a few possible orientations relative to the surface [169]. Additional orientations must be considered for more complex molecules.

Leenaerts *et al* used DFT to investigate the interaction between pristine graphene and 5 gaseous molecules: H₂O, NH₃, CO, NO₂, and NO [165]. The adsorption energy, distance from the graphene surface, orientation, and charge transfer was calculated for each molecule. They found that H₂O and NO₂ act as p-type dopants, with NO₂ showing the greatest charge transfer from the surface. NH₃, CO, and NO act as n-type dopants.
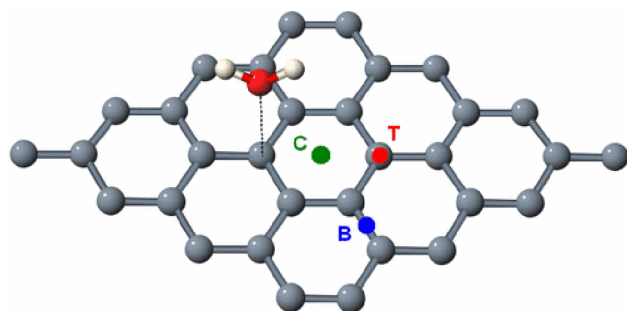
Figure 10. The adsorption sites of gases on graphene. The three potential sites of adsorption on graphene are above a carbon (T), between two carbons (B), and in the center of a carbon ring (C). Reprinted figure with permission from [165], Copyright 2008 by the American Physical Society.

Zhang *et al* investigated graphene for sensing many of the above molecules [170]. They computed the adsorption energy and charge transfer of each molecule on graphene doped with P, B and N, and on graphene containing vacancies. They found that graphene with vacancies had the greatest adsorption energy for all molecules except NH_3, which bound tightest to B-doped graphene.

NH_3 and NO_2 have been found to remain as n-type and p-type dopants, respectively, regardless of the condition of the graphene sheet. CO is shown to have very little interaction with doped graphene, but acts as an n-type dopant on graphene with vacancies. NO acts as a slight to moderate n-type dopant for doped graphene, matching its behavior in pristine graphene, but behaves as a significant p-type dopant on graphene with vacancies [170].

6.2.2. Transition metal dichalcogenides. The majority of research into how gaseous molecules affect the properties of transition metal dichalcogenides has been in the context of photo-luminescent devices. In a recent paper by Liu *et al*, the impact of oxygen on MoX_2 and WX_2 monolayers was simulated using DFT [171]. They found that pristine monolayers were unaffected by the presence of oxygen. However, oxygen molecules have significant interaction with single chacolgenide vacancy defects, which is a very common defect in MoS_2 monolayers [172–174].

Their results show that for MoX_2 and WX_2 (X = S, Se), O_2 molecules adsorb onto vacancy sites, flattening the highest valence band and increasing the effective mass of the holes compared to the pristine monolayers [171]. In $MoTe_2$ and WTe_2, O_2 was found to dissociate across the monolayer with one oxygen filling the vacancy and another bonding with a chalcogen atom. The resulting band structure shows that the electronic properties of these two monolayers is largely unaffected by oxidation, making them ideal for device fabrication. The band structures of MoS_2 under all these scenarios are illustrated in figure11.

Oxygen can also dissociate across the other TMDCs, resulting in only slightly influenced electronic properties. However, thermal annealing is required to overcome the energetic barrier in most cases [171]. In both adsorbed and dissociated

cases, the defect state introduced by the chacolgen vacancy disappears.

Tongay *et al* found that nitrogen gas impacted the band structure of MoS_2 during photoluminescence experiments and investigated further using DFT simulations [175]. They found that, similar to Liu *et al*, N_2 physisorbs only onto defect sites in MoS_2 at sulfur vacancies and di-vacancies, and that the defect states introduced by the vacancies disappeared when the N_2 interacts with the defects. In addition, the defect sites screened excitons when in vacuum, but after introducing N_2 to the system the free and bound neutral excitons were stabilized and contributed to the photoluminescence spectrum.

Interaction between monolayers and H_2O has been considered in section 6.1. However, the context of that interaction is in regard to electrochemistry. Molecules of H_2O are present in air, and thus should be considered when determining monolayer behavior. As has been the trend so far, the molecule is found to interact strongly with sulfur defects in MoS_2 [174]. The charge transfer from the monolayer to the molecule increases by a factor of 5 when comparing the adsorption to a pristine monolayer and a sulfur vacancy. The exact impact on the band structure was not explored, but it was found to improve the photo-luminescent intensity of MoS_2 by a factor of ten.

7. Electronic properties

7.1. Band structure

In a semi-infinite system where atoms are isolated from each other, all electrons have the same atomic energies. As the interaction among atoms increases and the atomic orbitals overlap, the energy levels hybridize and form continuous bands. However, the dimension of the material has an impact on the energy levels. When confining the system in any given direction, band energies are generally separated by quantized energy separations in a phenomenon known as quantum confinement. As a result, band gaps can appear in 2D materials derived from bulk metals, and band gaps can increase in 2D materials derived from bulk semiconductors or insulators.

These bands can be calculated using *ab initio* methods. The three most common methods are DFT with PBE functionals [82], HSE hybrid functionals [86] as introduced in section 3, and the *GW* approximation. A comparison of the band gaps and edges calculated with these methods can be seen in figure 12 for SnS_2.

As discussed in section 3, semi-local DFT functionals typically underestimate the band gap. Consequently, of the above methods, PBE yields the least accurate band gaps with an, on average, 50% underestimation as compare to experiment [176, 177].

The HSE06 hybrid functional offers significant improvement compared to PBE. HSE06 includes a percentage of the short-range Hartree–Fock nonlocal exchange energy of Kohn–Sham orbitals and potential energy of exchange-correlation, while long range Hartree–Fock exchange energy is derived from the exchange-hole formalism of PBE. HSE06
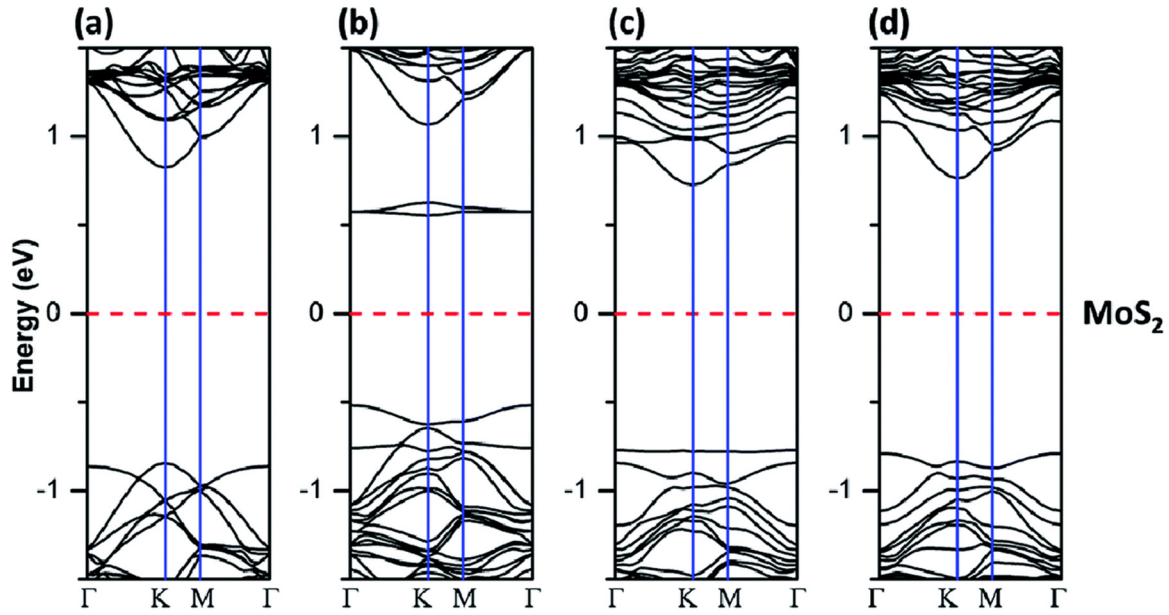
Figure 11. The band structure of MoS$_2$ under varying conditions. (a) represents the band structure of pristine MoS$_2$. (b) is the band structure when an S vacancy is present. (c) is the band structure when an O$_2$ molecule is adsorbed to the defect. (d) is when the O$_2$ is separated into 2 oxygen atoms that adsorb to the monolayer surface. The defect states that decrease the band gap in (b) disappear when O$_2$ adsorbs. Adapted from [171] with permission of The Royal Society of Chemistry.
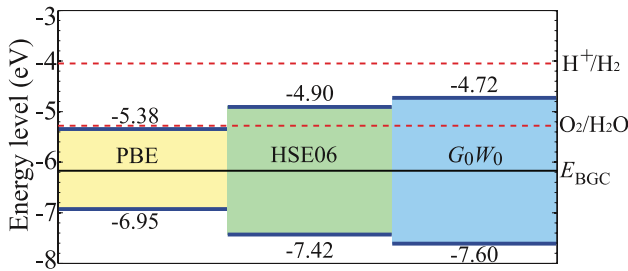

Figure 12. The calculated band edges of SnS$_2$ using PBE, HSE, and *GW* methods. The more accurate the method the larger the predicted band gap. The HSE band gap is 60% larger than the PBE, while the G_0W_0 band gap is 14% larger than the HSE. Reprinted figure with permission from [178], Copyright 2013 by the American Physical Society.

functional still, on average, underestimates bandgap energy, but is significantly closer than the PBE functional.

The *GW* methods predicts a band gap very close to experiment. In this method, starting from a converged Kohn–Sham DFT band structure, the RPA screened Coulomb interaction *W* is used to construct the exchange self-energy diagram $G \cdot W$, giving rise to a dynamical potential for the single electron Green's function *G*. The method approximates the Hedin equations by replacing the interacting electron vertex with the bare one and, in some flavors, omitting self-consistence.

There are three flavors to computer implementation of *GW* method: *G0W0*, *GW*0 and pure *GW* [94]. The *G0W0* approach holds the Green's function *G* and screened Coulomb's potential fixed across iterations, leading to a non-self-consistent solution. On the other hand, *GW*0 iterates over *G* while it keeps *W* constant, which gives the partially self-consistent solution that matches the experimental data the best. Pure *GW* method iterates over both *G* and *W*, which yields completely self-consistent solutions. This method

gives similar results to *GW*0, but is significantly more computationally expensive.

The effective mass of electrons can be approximated in the same way as in a bulk geometry. In the general case, the electron accelerate according to the mass tensor

$$M_{i,j0}^* = \hbar^2 (\mathrm{d}^2 E/\mathrm{d}k_i \mathrm{d}k_j)^{-1}, \qquad (3)$$

while in some cases where the band structure is isotropic, the above simplifies to the relation $m_0^* = \hbar^2/(\mathrm{d}^2 E/\mathrm{d}k^2)$. Knowing the effective mass of an electron and hole in a 2D material is useful for numerous applications, especially when building electronic devices. Having a lower effective mass allows for faster electron transport, and thus improved functionality from the device. The accuracy of the effective mass is dependent on the accuracy of the methods used to calculate the bands. For example, *GW* is able to include dynamic Coulomb interaction effects not captured in PBE or HSE functionals, potentially changing the curvature of the bands.

7.2. Optical absorption and excitations

7.2.1. Fundamentals of light absorption. Light absorption and emission by a material requires conservation of energy, momentum, angular momentum, and spin. In the optical range of the spectrum, transitions must conserve energy in the eV range, i.e. typical optical transitions involve electronic excitations between filled and empty states. Since the photons carry very little momentum, the change in momentum of the electron is negligible unless phonons are involved in the transition. This means optical transitions occur vertically between occupied and empty states in the band structure, else they require the emission or absorption of a phonon. During an optical transition, the electron spin must be preserved when spin–orbit interactions are negligible. The magnetic quantum
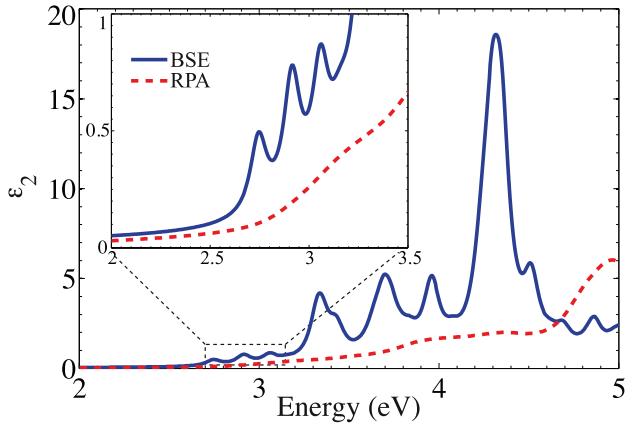
Figure 13. Calculation of the exciton binding energy in 2D SnS$_2$ using the BSE. The inset shows a close-up of the imaginary part of the permittivity, ϵ_2 with three exciton peaks. To compensate for the bandgap underestimation using the PBE functional in the RPA calculation, the spectra are shifted by 1.0 eV, which is the difference between the HSE06 and PBE bandgaps. Reprinted figure with permission from [178], Copyright 2013 by the American Physical Society.

number must either remain the same or change by one, and the angular momentum quantum number must change by one. With these rules, which optical transitions are allowed can be calculated and be used to characterize the optical properties in materials [179].

Following the excitation of an electron from a filled valence band state into an empty conduction band state by absorption of a photon, the electron will eventually relax to lower energy states. This relaxation can occur in two ways: radiatively or non-radiatively. The former results in light emittance and is often independent of phonons. The latter requires phonon emission to dissipate the energy and change the momentum. Radiative processes can also involve phonons, though the rate of these processes is typically smaller than for direct transitions.

When an electron is optically excited across the band gap of a material, the resulting hole state in the conduction band interacts with the electron in the valence band state. The bound state between the electron and hole is called an exciton. These excitons can either be localized at crystallographic sites, so-called Frenkel excitons, [180] or freely move through the material as so-called Wannier-Mott excitons [181]. Furthermore, excitons can exhibit a net positive or negative charge, which occurs when an additional hole or electron, respectively, binds with the original electron-hole pair to form a trion [182, 183].

Since the Kohn–Sham equations of DFT map the electronic system onto a system of non-interacting electrons, other computational methods and corrections are necessary to accurately calculate the properties of excitons, which are inherently interacting two-particle excitations. Thus, *GW* methods and BSE calculations are often used to determine optical absorption and emission properties and exciton binding energies. As an example, figure 13 shows that the binding energy for the exciton in 2D SnS$_2$ calculated with the BSE is 0.4 eV [178].

The computational expense of the BSE makes routine calculations of the exciton binding energy difficult. To estimate the exciton binding energy, the Mott–Wannier model [184] can be applied to 2D materials [178, 185]. This model approximates the exciton binding energy as the binding energy between an electron and a hole embedded in a dielectric continuum. In two dimensions, the first excitonic binding energy is

$$E_0 = 4\frac{m_r}{m_0}\frac{R_\infty}{\epsilon_{2D}^2}, \tag{4}$$

where m_r is the reduced effective electron mass, m_0, the rest mass of the electron, ϵ_{2D} the effective permittivity, and R_∞ the Rydberg constant [184]. For 2D systems, care must be taken in the calculation of the permittivity tensor to account for the size of the simulation cell, i.e. the thickness of the vacuum layer [178]. The contribution of the vacuum to the computed permittivity tensor elements can be corrected using the linear law, $\epsilon_{calc} = f\epsilon_{2D} + (1f)\epsilon_{vac}$, where f is the volume fraction of the 2D structures in the simulation cell, $\epsilon_{vac} = 1$ is the permittivity of vacuum, and ϵ_{2D} is the permittivity of the 2D material [178].

For SnS$_2$, the exciton binding energy predicted from the Mott–Wannier model is identical to the binding energy calculated by solving the BSE. While such perfect agreement is probably fortuitous, it nevertheless indicates that the simple approximation can provide insight into the excitonic properties of 2D materials [70].

7.2.2. Photonic devices. Graphene absorbs 2.3% of visible light, [187] which is surprisingly high considering its only one atom thick. TMDCs have shown even higher amounts of absorption, ranging from 5-10% depending on the wavelength [188]. Combined with the flexibility of 2D materials, this has led to investigations into their potential in photovoltaic [189, 190] and luminescent devices [175, 186, 191]. These behaviors are intrinsically linked due to the above transition rules dictating both processes. At present, these materials do not outperform those in commercially available devices.

It has been found that excitons dictate the optical emission spectra of 2D materials. For photoluminescence (PL) based electronics using 2D materials, both WS$_2$ [186] and MoS$_2$ [175] have had their photo-luminescent spectra measured before and after the introduction of point defects. Prior to defect introduction, the spectra are largely dominated by a peak corresponding to a negative trion in MoS$_2$ and a mixture of trion and neutral exciton contributions in WS$_2$. As point defects are introduced to the monolayers, a lower energy peak associated with defect bound excitons arises. A higher energy peak associated with neutral excitons appears to envelop the trion peak, and the overall PL increased as more defects were introduced. In WS$_2$, the trion contribution is found to disappear almost entirely. The spectral contribution of each exciton after different plasma times, i.e. with increasing defect density, can be seen in figure 14.

Electroluminescence (EL) is also feasible through heterostructure design. Withers *et al* developed graphene|*h*-BN|MS$_2$| *h*-BN|graphene (M = Mo,W) heterostructures
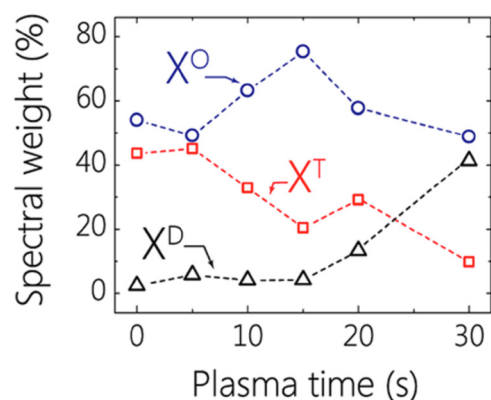
Figure 14. The spectral contribution of excitons to the emission spectra of monolayer WS_2 as plasma time, the source of defect generation in the monolayer, increases. As plasma time increases and more defects are present, the contributions by the negative trion contribution (X^T) decreases, by the neutral exciton (X^0) fluctuates somewhat, and by the defect bound excitons (X^D) increases significantly. Reprinted (adapted) with permission from [186]. Copyright 2015 American Chemical Society.

Table 1. First-principles simulations have been used to predict several 2D photocatalysts.

2D Material	References
CrS_2	[36]
HfS_2	[201]
$(N_2H_4)_2Mn_3Sb_4S_8(\mu_3\text{-OH})_2$	[202]
MS_2 (M = Mo, *W*, Pt) and $PtSe_2$	[203]
MX (M = Ga, In; X = S, Se, Te)	[204]
MX (M = Ge, Sn, Pb; X = O, S, Se, Te)	[131, 205]
CdX (X = S, Se, Te)	[206]
TcX_2 (X = S, Se)	[207]
MPX_3 (M = Zn, Mg, $Ag_{0.5}Sc_{0.5}$, $Ag_{0.5}In_{0.5}$; X = S, Se)	[208]
$MPSe_3$ (M = Fe, Mn)	[209]
$AlSiTe_3$, $InSiTe_3$, Al_2Te_3, B_2S_3, As_2X_3 (X = S, Se, Te)	[19]
β-MNX (M = Zr, Hf; X = Cl, Br)	[210]
α-MNX (M = Zr, Hf; X = Cl, Br, I)	[210]
TiNM (M = Cl, Br)	[211]
BiOX (X = Cl, Br, I)	[212, 213]
Zr_2Co_2, Hf_2Co_2	[214]

which displayed EL spectra nearly matching the PL spectra of the isolated monolayers [191]. These devices operate by electrons and holes tunneling from the metallic leads (graphene) through a thin tunneling junction (*h*-BN) into a semiconductor with a band gap in the visible range (MS_2). Like in the PL device, it is found that the trion and bound neutral defects dominated the emission spectra of the device.

In summary, excitons are crucial to the optical behavior of 2D materials. However, accurately predicting how monolayers will respond to optical excitation is difficult at this time due to the computational costs. Simulating excitons and point defects both have increased computational expenses, which is compounded when both are simulated at once. These calculations are within the realm of possibility on an individual basis, but high throughput simulations of this nature are difficult at this time.

7.3. Work function/ionization potential

The work function of a solid is the energy it takes to move a single electron from the surface to a point far outside the solid. 'Far' means here that the distance is large enough to suppress the local interaction with the surface but small enough to feel the macroscopic electro-magnetic fields of the solid. This definition is to make the work function a property of the surface only [192]. For 2D materials, the work function can be easily calculated. After converging the size of the vacuum, the local potential will reach a maximum in-between periodic replica which represents the vacuum according to the above definition. One can then find the difference between the Fermi level and the vacuum level to resolve the work function of the material.

7.4. Photocatalysis

One of the applications where two-dimensional materials have demonstrated the potential to outperform bulk materials

is that of photocatalytic water splitting to derive hydrogen as a fuel [51]. Solar energy fuel generation provides a route to clean, environment friendly, and renewable energy production, but its practical application has been largely limited by poor efficiency of solar energy conversion [193, 194]. 2D materials present two intrinsic advantages in comparison to other nanostructures and bulk materials which enhance their photocatalytic efficiency. First, they exhibit high specific surface area for the redox reactions. Second, the photogenerated electrons and holes migrate to the surface more quickly due to the reduced dimensionality in the third direction, potentially reducing electron-hole recombination, thus increasing efficiency. In addition, 2D materials represent a large exploratory space of materials with tunable electronic, mechanical, and optical properties [17, 37].

There have been several experimental validations of enhancement in photocatalytic water splitting efficiency with the reduction in dimensionality in the vertical direction. For instance, freestanding single-layer SnS_2 is observed to provide high photocurrent density of 2.75 mA cm^{-2}, over 70 times higher than that of bulk SnS_2. In addition, it has an incident photon to converted electron ratio (IPCE) of 38.7% at an irradiation wavelength of 420 nm, in contrast to only 2.33% for bulk SnS_2 [195].

In another example, ZnSe with four atomic layers exhibits a photocurrent density of 2.14 mA cm^{-2}, about 200 times higher than the value for bulk ZnSe and an IPCE of 42.5% compared to 0.25% of the bulk counterpart [196]. Similar photocatalytic enhancements through the reduction of the dimensionality have been observed for other single and few-layer 2D materials such as SnO, SnS, SnSe, CdS, and WS_2 [195–200].

Theoretical investigations have been successful in identifying several potential photocatalysts by searching for 2D materials which have properties suitable for photocataytic water
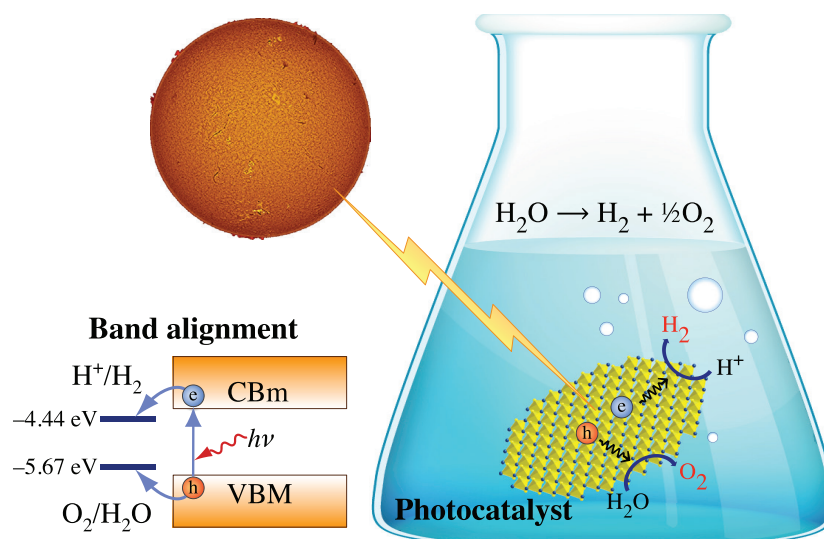
Figure 15. Schematic mechanism of photocatalytic water splitting. The minimum criteria for potential photocatalysts to show activity towards water splitting are (a) presence of a band gap larger than free energy of water splitting, 1.23 eV, (b) stability in water, and (c) the band edges of the photocatalyst should straddle the redox potentials of hydrogen and oxygen evolution. Reprinted with permission from [51]. Copyright 2015 American Chemical Society.

splitting. More than 50 2D materials have been predicted to show photocatalytic activity for water splitting, Table 1. The intrinsic properties which are desirable in a potential photocatalyst include, but are not limited to, a) high thermodynamic stability, b) a band gap larger than the free energy of water splitting, c) large visible light absorbance efficiency, d) suitable band edge alignment with respect to redox potentials of hydrogen and oxygen evolution reactions, and e) stability in water; [51, 215] see figure 15. In addition, application of strain, chemical bias, and doping have been shown to enable the engineering of key photocatalyst properties such as band edge locations, band gap sizes, and optical spectra.

While several studies have explored the use of 2D materials as catalysts for hydrogen production, similar investigations focused on reduction of CO_2 for fuel generation have been limited. Recently, Liang *et al* have shown that single unit-cell Bi_2WO_6 layers can reduce CO_2 to produce 75 μmol g^{-1} h^{-1} of methanol, which is 125 times higher than that of bulk Bi_2WO_6. Apart from identifying potential photocatalysts, challenges in the generation of carbon-based fuels include the mitigation of low efficiencies due to loss of excitons to hydrogen generation and low product selectivity due to comparable redox potentials of the closely competing final reduction products.

7.5. Magnetic insulators

As outlined in section 8, some 2D materials display a net magnetic moment. When such monolayers also have a band gap, the band structure differs from non-magnetic insulators. The magnetism results in two sets of bands in the monolayer's electronic structure: one for up spin electrons, and one for down spin electrons. As stated in section 7.2, electron spin must be preserved as an electron transitions from one band to another. This results in one band gap for up spin electrons, and different gap for down spin electrons.

One can use such materials in spintronic applications. Since there are two different band gaps, electrons in one spin channel often have a higher chance of exciting across the gap than electrons of the opposite spin. As a result, it is theoretically possible to build a transistor that improves its on/off current ratio by using a magnetic insulator. Combined with the small size of monolayers, this technology has the potential to significantly increase the performance of electronic devices and such materials are of great interest to spintronic research.

7.6. Half-metals

Naturally, magnetism can also affect the bands in 2D metals. A standard ferromagnetic 2D material is one in which the two spin channels are metallic but not energetically degenerate. In some cases, however, one spin develops a band gap while the other remains metallic. Such materials are called half-metals, and an example of such a band structure is shown in figure 16. The band structure shown in figure 16 was calculated with the PBE functional, however, it has been demonstrated that HSE or other more accurate functionals are required to adequately assert the presence of a half-metallic band structure [216].

Half-metallic behavior has recently been discovered in pristine 2D $FeCl_2$, $FeBr_2$, and FeI_2, all in the $1T$ structure [216, 217]. It is understood that the half-metallic behavior in these materials strictly depends on their reduced dimensionality, since their multilayer forms have an interlayer antiferromagnetic (AFM) order [218]. Their half-metallic nature makes these materials very promising for spintronic applications. Designing a magnetic tunnel junction with half-metallic leads, in principle, enables the use of 100% spin-polarized currents, and in turn creates a very high ratio between the junction's on and off states.
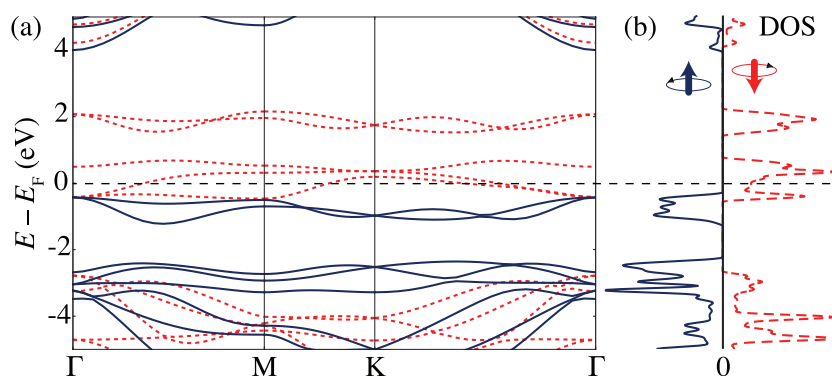
Figure 16. The PBE band structure and density of states of the $FeCl_2$ half metal. The solid blue lines represent the majority spin component and the dashed red lines the minory one. The minority spin electron bands cross the Fermi level and thus behave metallically, whereas the majority spin electrons exhibit a band gap. Reprinted figure with permission from [17], Copyright 2017 by the American Physical Society.

8. Intrinsic magnetism

8.1. Computational treatment of magnetism

Spin-polarized DFT can be employed to compute various magnetic properties of a 2D magnetic material. An initial guess at each atom's magnetic moment is required, and can typically be estimated using Hund's rule. During a self-consistent DFT calculation, the magnetic moment on each atom is optimized as the wavefunctions are determined.

For a ferromagnetic (FM) 2D material, a single unit cell is sufficient to describe the magnetic configuration. In contrast, calculations of antiferromagnetic (AFM) materials often require supercells. This is to allow for various distributions of up and down spins across the material. For example, Sivadas *et al* considered three types of AFM structures in 2D $CrSiTe_3$: Néel, zigzag, and striped [219]. This is an example of how a complete assessment of antiferromagnetism in a material is more complicated and computationally expensive than that of ferromagnetism.

Having obtained the ground state magnetic structure, it is worthwhile understanding the underlying mechanism that causes the magnetic ordering. Depending on whether the system is metallic or semiconducting, the Stoner and Heisenberg exchange models are respectively useful for understanding the exchange interactions.

The magnetocrystalline anisotropy energy (MAE) is an important parameter that should be calculated. This is because a significant MAE is required for a 2D system to exhibit a long-range order, which is deemed impossible according to Mermin and Wagner [2]. That said, there exist two notable exceptions to the applicability of the Mermin–Wagner theorem: the Ising and the Berezinsky–Kosterlitz–Thouless systems, [220] both of which exhibit sizable MAEs. The MAE can be calculated by the torque method [221] via non-collinear calculations including spin–orbit coupling. In these calculations, the spin directions are fixed while the magnetic moments are optimized. This allows one to plot the energetic stability of the material as the magnetic moment points in various directions, and thus find which direction is the ground state. If the magnetic moment is equally stable in every direction in the plane of the monolayer, it is considered an 'easy plane'. If the most stable position is perpendicular to the plane, it is considered an 'easy axis' monolayer.

8.2. Ferromagnetism, anti-ferromagnetism, ferrimagnetism

Existence of magnetic order offers an additional degree of freedom for controlling electrical properties of 2D materials. As such, magnetic 2D materials hold great promise for applications in novel electronic devices. Recently, a number of 2D materials have been predicted via DFT calculations to exhibit ferromagnetic and antiferromagnetic order. These 2D materials are often binary compounds consisting of transition-metal and chalcogen elements such as VS_2, MnS_2, $MnSe_2$, and FeS_2 [222–224]. Ternary compounds form a separate group of magnetic 2D materials with a general chemical formula of ABX_3 (A = V, Cr, Mn, Fe, Co, Ni, Cu, Zn, B = P, Si, Ge, Sn, and X = S, Se, Te) [219, 225–227]. It is worth emphasizing that most of the above mentioned 2D materials possess an interesting combination of magnetic order and semiconducting properties. The critical temperature (Curie or Néel) of the predicted magnetic 2D materials can range from a low temperature (e.g. 90 K for 2D $CrSiTe_3$ [226]) to several hundred Kelvin (e.g. 675 K for 2D CrN [228]), computed based on Monte Carlo simulations.

The interest in magnetic 2D materials is not only reflected by emerging theoretical studies. Experimental groups have also provided evidence of magnetic order in 2D materials. For example, Gong *et al* confirmed the intrinsic long-range ferromagnetic order in 2D $CrGeTe_3$ via scanning magneto-optic Kerr microscopy [229]. Another recent experiment performed on monolayer chromium triiodide CrI_3 reported intriguing magnetic properties that are strongly dependent on the number of monolayers [230].

8.3. Anisotropic magnetism

In addition to magnetic order, magnetocrystalline anisotropy (mainly due to spin–orbit coupling) is another critical property that could widen the applications of magnetic 2D materials. Here, DFT simulations play similarly important roles in computationally identifying potential magnetic 2D materials
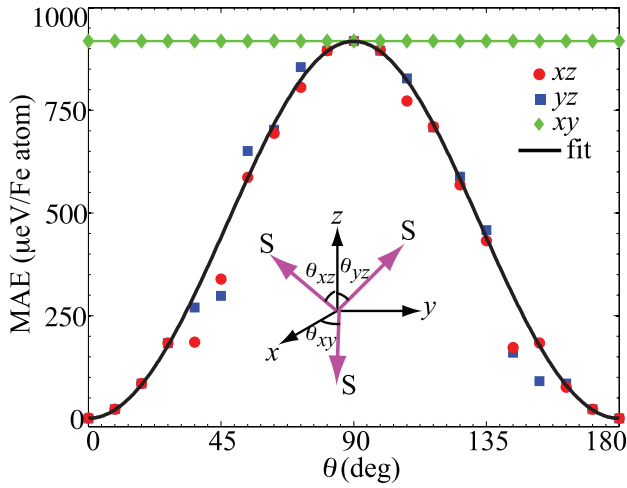
Figure 17. Magnetic anisotropy energy in FeGeTe₃. As can be seen, the *z* direction is most stable for the direction of the magnetic moment in the monolayer, while in-plane rotation has no barrier. Reprinted figure with permission from [231], Copyright 2016 by the American Physical Society.

with strong magnetocrystalline anisotropy. For instance, Zhuang *et al* have shown that single-layer FeGeTe₃ exhibits a significant magnetocrystalline anisotropy energy (MAE, see figure 17), which make this single-layer material potentially useful for magnetic recording applications [231]. It is natural to expect that more theoretical efforts will be spent searching for new 2D materials with strong magnetocrystalline anisotropy capable of withstanding thermal fluctuations at high temperatures.

9. Superconductivity

According to the Mermin–Wagner theorem [2] a 2D system cannot become superconducting because the long range fluctuations of the spontaneously broken symmetry prevent the system from ordering. The symmetry in question for a superconductor is the electromagnetic gauge field which is reflected in the phase of the superconducting order parameter such that the response to such perturbations is expected to become strong in reduced dimensions and eventually suppress T_c completely.

Real 2D systems have a finite, albeit small, thickness and can undergo a quasi long range ordering, the Berezinsky–Kosterlitz–Thouless transition, and still superconduct. The question arises to what extent the increased susceptibility to fluctuations of the order parameter translates into an effective T_c reduction. To the best of our knowledge, first-principles calculations of phase and amplitude fluctuations have not been attempted so far. The calculation of T_c using the standard mean field Eliashberg equations while accurately treating the underlying electronic and phononic structure in a 2D geometry, however, indirectly also sheds light on the importance of fluctuation effects. The changes in the electronic and phononic structure can be important and in some cases are known to even increase T_c beyond the bulk value.

Here, we focus on a computational approach to the problem and, since the methods are by far more accurate, on electron–phonon driven superconductivity.

Phonon calculations are $\mathcal{O}(N_{atoms})$ more expensive than electronic structure calculations and thus free standing slabs and interfaces are not easy to compute accurately. Otherwise the approach is similar to other 2D material calculations. Most electronic structure codes work in 3D, so for a surface geometry the amount of vacuum between two slabs must be sufficient to reduce spurious interactions. This is of particular importance when unsymmetrical slabs are used where one has to make sure no artificial dipole interaction between periodic replica obscures the result. The slab size has to be large enough that the local chemical environment of the interface is converged, which can easily lead to unit cells with several dozens of atoms. Possible dangling bonds can be saturated with specifically designed H-like atoms to speed up the convergence with slab size. In spite of these challenges, there have been a number of first-principles calculations of electron–phonon driven superconductivity of systems in a surface and free standing layer geometry.

9.1. Pb monolayer on Si(1 1 1)

In an effort to study the approaching 2D limit of superconductivity by controlling the number of Pb layers on Si(1 1 1), Guo *et al* [232] found an oscillating behavior of T_c as a function of number of layers. This is attributed to the effect of quantum confinement of the electronic wavefunction, which creates oscillations in the density of states and the electron–phonon coupling with the vertical dimension. Yu *et al* [233] have studied a system of four to ten free standing layers of lead, also finding an oscillating behavior of the coupling constant and density of states. Note that while in bulk systems the effective screened Coulomb interaction μ^* is well approximated within the range 0.1–0.15, the screening in a 2D geometry is more difficult to compute [233]. Özer *et al* found a further reduction of T_c from 6.5 K at a thickness of 18 layers to 5 K upon decreasing the number of layers to five which excludes a final wetting layer [234]. This is also supported by DFT calculations, [233, 235] even though the details of the interface with Si(1 1 1) are neglected in these studies. A single layer of Pb on a Si(1 1 1) substrate has been fabricated by Zhang *et al* [236] and is superconducting with a $T_c = 1.86$ K for Pb in the striped incommensurate phase (SIC). Modeling the SIC phase by a $\sqrt{3} \times \sqrt{3}$ assembly, this T_c is well reproduced by a first-principles calculation by Noffsinger and Cohen [237].

9.2. Graphene related compounds

There have been a number of first-principles investigations of electron–phonon superconductivity in doped graphene [238–241]. The doping was achieved by including a Li coating in the calculations [238, 239]. Using parameters for the Coulomb screening from well studied bulk graphene intercalated materials, [239] predicted a transition temperature of 8.1 K; the experimental $T_c = 5.9$ K [242] was later discovered to be in fairly good agreement with this result.
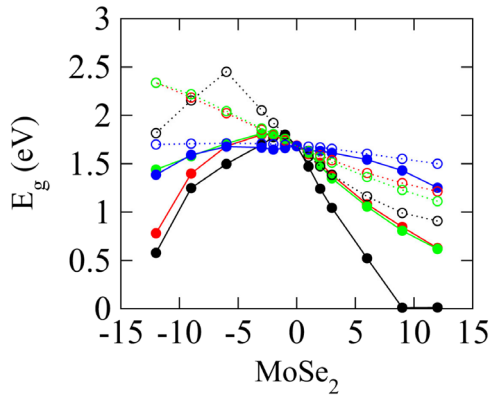
Figure 18. The change in band gap with applied strain of $MoSe_2$. Black represents isotropic strain, red and green represent uniaxial strain in perpendicular directions, and blue represents shear strain. Reprinted from [252], Copyright 2016, with permission from Elsevier.

9.3. FeSe on $SrTiO_3$

FeSe is a very interesting material with a bulk T_c of 8 K [243]. The discovery of superconductivity in a FeSe monolayer on $SrTiO_3$ [244] has caused enormous excitement in the community owed to the large T_c of 65 K in ARPES [245]. The hope is that understanding the origin of the greatly increased transition temperature could enable the construction of similar superconductors of even higher T_c and improved properties for technological applications. While bulk FeSe is generally considered a sign-changing $s_\pm$ superconductor driven by repulsive electronic interactions (see [246] for a review), measurements of the ARPES gap of FeSe on $SrTiO_3$ reveals a very isotropic s-wave gap [245]. Consequently, attractive interactions originating from electron–phonon coupling were investigated in the material [247]. So-called replica bands in ARPES suggest a strong coupling of the modes at $\boldsymbol{q} = \boldsymbol{0}$, [245] which has the particular feature that the electron–phonon coupling is supporting superconductivity in all pairing channels, including unconventional d and $s_\pm$ channels.

While FeSe appears to be only weakly bound to the substrate, an explanation for the strong electron–phonon coupling at small momentum involves the motion of the polar oxygen mode in $SrTiO_3$. The energy of this mode and the observed energy offset of the replica band are similar. First principles calculations have found this large coupling at $\boldsymbol{q} = \boldsymbol{0}$ [248] in agreement with the original model. That said, DFT calculations are not without problems. In many different types of DFT functionals, it is difficult to promote the charge transfer from $SrTiO_3$ to FeSe in a similar way as observed in experiment [249–251]. Moreover, and most importantly, the DFT bands at the Fermi level are in disagreement with experiment. This very interesting material is still not fully understood.

10. Responses to stimuli

Certain properties in 2D materials are only accessible in the presence of external stimuli. This section focuses on the responses of 2D materials to mechanical and electrical stimuli, and how to understand these responses computationally.

Methods to calculate relevant properties are discussed in their individual sections.

10.1. Mechanical stimuli

Strain engineering and response in 2D materials has been heavily studied [65, 252–260]. Properly understanding 2D materials' behavior under mechanical stresses requires a slightly different treatment than bulk materials. Stress and strain along the z direction in monolayers is rarely considered, which reduces the dimensionality of the resulting property tensors. Thus, there are only three kinds of stress in 2D materials: normal stress in the x direction, normal stress in the y direction, and shear stress in the x–y plane.

10.1.1. Band structure.
Strain typically shifts the electronic bands in materials, most notably growing or shrinking band gaps. Graphene is well known for developing a band gap upon large enough applied strain [253–255], and suffering a resulting decrease in conductivity [256]. Similarly, MX_2 (M = Mo, W, X = S, Se, Te) monolayers have been observed to undergo changes in conduction band minimum (CBm) and valence band maximum (VBM) locations under strain [252, 257–259]. This behavior is a result of the orbitals contributing to the band structure responding to the strain. Electronic bands do not always uniformly change with applied strain, nor is their response necessarily isotropic with regard to the direction of applied strain. The response of the $MoSe_2$ band gap to strain is shown in figure 18.

10.1.2. Elasticity.
Elasticity is a material property that relates a mechanical stress to a strain response, and vice versa. Elastic constants can be estimated for 2D materials using a variety of computational methods. A common approach is to use the finite differences method, [265] which measures changes in stress due to small changes in applied strain on a unit cell. The relaxed ion elastic constants, which include ionic and electronic contributions, are then reported in a tensor.

All elastic constants for 2D materials have different units than those for 3D materials. Due to the reduced dimensionality, a force or displacement is applied along a unit of length rather than a unit of area. Elasticity or stiffness coefficients have units of N m^{-1} as a result. In VASP, 2D constants can be derived by normalizing the calculated 3D constants with the c lattice parameter. Elastic constants typically converge within at least 1% at a z spacing of 15 Å [262].

Graphene is known for its high elastic coefficient of 350 N m^{-1}, [266] though 2D materials have a wide range of elastic constants. The elastic constants typically range between 30 and 300 N m^{-1}, and shear constants are between 10 and 70 N m^{-1} [262]. The elastic coefficient of h-BN is also large at 297 N m^{-1}. 2D materials with low elastic coefficients include tetragonal PbO (34 N m^{-1}) and buckled hexagonal InSb (28 N m^{-1}).

10.1.3. Piezoelectricity.
Piezoelectricity is a property that quantifies the interaction between mechanical stress or strain and electric fields generated by the material. The phenomenon
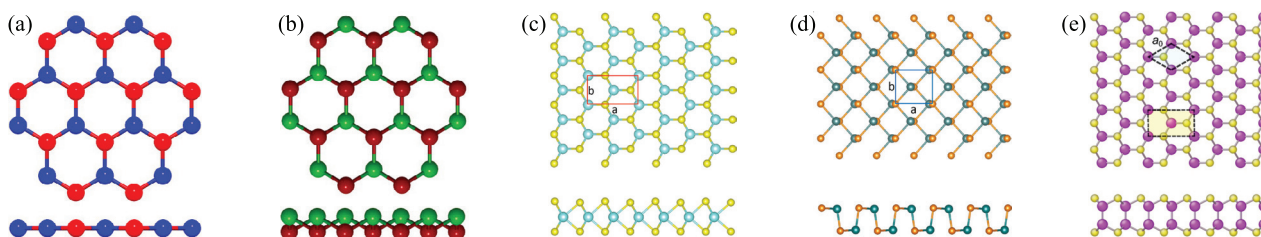
Figure 19. Known piezoelectric structures: (a) planar honeycomb structure of $h-$BN, (b) buckled honeycomb structure of III–V compounds, (c) $2H$ structure of transition metal dichalcogenides, (d) distorted rocksalt structure of group-IV chalcogenides, and (e) hexagonal structure of group-III monochalcogenides [261]. Image sources: (a) and (b) Reprinted with permission from [262]. Copyright 2015 American Chemical Society. (c) and (d) Reprinted with permission from [263]. Copyright 2015, AIP Publishing LLC. (e) [264] © Tsinghua University Press and Springer-Verlag Berlin Heidelberg 2015. With permission of Springer.

only arises in materials without inversion symmetry, as applied strain causes species of differing electronegativity to distribute unevenly, resulting in the formation of a dipole and thus a net electric field across the material. There are five known classes of 2D materials that break inversion symmetry: planar and buckled hexagonal group III–V semiconductors, [262, 267] $2H$ transition metal dichalcogenides, [7, 8] group III monochalcogenides, [264] and group IV monochalcogenides [268]. These monolayers are shown in figure 19.

Similar to elastic tensor coefficients, piezoelectric coefficients in 2D materials have different units due to reduced dimensionality. The units of the polarization density P is reduced to C m^{-1}, and therefore the piezoelectricity tensor, $e = dP/d\epsilon$, has units of C m^{-1}. The piezoelectric tensor, $d = dP/d\sigma$, is normalized by the 2D elastic tensor and maintains its units of m V^{-1}. These tensors can be calculated using density functional perturbation theory [262, 269–272].

An important distinction between piezoelectricity and elasticity is that electrical responses are not limited to the x–y plane for 2D materials [262]. This allows piezoelectric 2D materials to exhibit out-of-plane electrical responses due to in-plane stresses. Buckled hexagonal structures have been identified to exhibit an out-of-plane piezoelectric coefficient, which range from 0.05–0.5 pm V^{-1} [262]. It should be noted that all of the known buckled hexagonal structures are either unstable or metastable relative to other 2D phases [35].

Piezoelectric coefficients, particularly those in buckled crystal structures, have been shown to converge more slowly than elastic constants. It is computationally expensive to calculate accurate coefficients using a large z spacing, but coefficients can be estimated by extrapolating to infinite z spacing. A recent study extrapolates in-plane coefficient e_{11} by fitting values to the inverse of the layer spacing and out-of-plane coefficient e_{31} by fitting values to the square inverse of the layer spacing [262].

In-plane 2D piezoelectric coefficients are usually in the range of 1–10 pm V^{-1}. The largest coefficients are typically in metal oxides such as CdO (21.7 pm V^{-1}) and ZnO (8.65 pm V^{-1}) and in metal dichalcogenides such as CrTe$_2$ (13.45 pm V^{-1}) and CrSe$_2$ (8.25 pm V^{-1}) [262]. For more information on piezoelectric monolayers, we direct readers to a recent review of piezoelectric monolayers published by Zhang *et al* [261].

10.1.4. Magnetostriction. Magnetostriction is a magnetic analog to piezoelectricity. Magnetostriction was first observed in single

layer Fe$_3$GeTe$_2$, which exhibits a decreasing magnetic moment under compressive strain and an increased magnetic moment under tensile strain [231]. This was calculated using static calculations for applied biaxial strain ranging from -4% to 4%.

The degree of coupling is described by the magnetostrictive coefficient λ. This value depends on two components: the mangetoelastic energy density MAE, and the 2D elastic stiffness coefficient. For Fe$_3$GeTe$_2$, $\lambda = -559$ ppm (parts per million), which is found to be larger than known bulk Fe$_{1-x}$Ga$_x$ alloys [273]. The details of this calculation for hexagonal crystals is outlined by Cullen [274].

10.2. Electrical stimuli

The properties of 2D materials also frequently respond to external electrical stimuli. Some of the most interesting and technologically important responses are discussed below.

10.2.1. Thermoelectrics. A recent topic of research in 2D materials is thermoelectricity. Thermoelectric devices directly generate a voltage from a temperature gradient and vice versa, which makes them useful in several applications. These include cooling, sensors, and thermal energy harvesting.

The origin of the thermoelectric effect lies in differences of the conductivity of high energy versus low energy electric carriers such that in the hotter side of the material, where carriers are excited to higher energies, the diffusion to the colder side overcompensates the back-flow at lower energies. The most promising monolayer in the field at this time is black phosphorous due to its electronic and thermal anisotropy. One of the limiting factors in thermoelectric materials is that thermal and electrical conductivity often have positive correlation. In an ideal thermoelectric material, electrons will flow freely while a strong thermal gradient is preserved.

Black phosphorous not only has anisotropic electrical and thermal conductivities, but also preferred flow in orthogonal directions [275]. The electrical conductance has preferred transport along the armchair direction due to lower effective mass while the heat is transported along phonons which prefer the zigzag direction in black phosphorous. Through doping, black phosphorous becomes an extremely competitive material for use in thermoelectric devices. Its properties are illustrated in figure 20.

In order to determine the directions of flow for electrical and thermal conductivity, the band structure and phonon
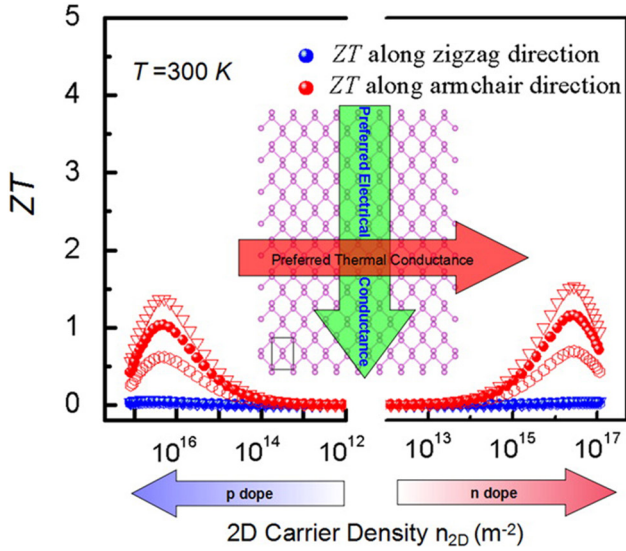
Figure 20. The thermoelectric behavior of black phosphorous, doped with carrier doping of approximately 2×10^{16} m^{-2}. The ZT, or measure of effectiveness as a thermoelectric, is found to increase with doping along the armchair direction while remaining low along the zigzag direction. This is a result of the anisotropic electrical and thermal conductivities in monolayer phosphorous. The open circles, closed circles, and inverted triangles represent phonon relaxation times of 150, 60, and 45 ps respectively. Reprinted with permission from [275]. Copyright 2014 American Chemical Society.

spectra for black phosphorous was calculated and analyzed for, respectively, effective masses and speeds of sound. For more information on thermoelectricity in 2D materials, we direct readers to the review by Zhang *et al* on thermoelectricity and its applications in 2D materials [276].

10.2.2. Ferroelectrics. Ferroelectric 2D materials have been elusive, in part because they require a lack of inversion symmetry to generate a net dipole in the material. This net dipole must also be able to have its direction changed, and maintain the change in direction after the applied field is removed. Further, materials that behave as ferroelectrics in their bulk forms do not necessarily retain their ferroelectric properties when their thickness decreases to the nanoscale. Nevertheless, layered ferroelectrics are a natural starting point when looking for ferroelectric monolayers.

CuInP$_2$S$_6$ (CIPS) is a layered ferroelectric material that is found to retain its ferroelectric behavior when decreased to a thickness of two monolayers [277]. When the polarization of the CIPS structure was calculated using DFT, it was found that the material remained ferrielectric as a bilayer. Although the mechanism that gives rise to its ferrielectricity is slightly different than that of conventional ferroelectricity, the response behavior for both is the same.

A monolayer that displays ferroelectric behavior in its most stable configuration was recently discovered computationally in the MXene Sc$_2$CO$_2$. This material displays both an in-plane and out-of-plane polarization, and was found to have an intermediate antiferroelectric phase, allowing for the transition from one out-of-plane polarization to the other. Group IV chalcogenides have also recently been found to be

multiferroic, displaying both ferroelectric and ferroelastic behavior [268].

Determining ferroelectric behavior computationally requires three steps: identifying a net polarization in the monolayer, identifying stable ferroelectric and antiferroelectric phases of the monolayer, and calculating the energetic barriers between the the phases. The first and second step can be found using standard DFT and Berry phase calculations. Determining the energetic barriers is best done with density functional perturbation theory. In addition, one must ensure that there is not a point during the transition when the material becomes metallic, or else the polarization is not guaranteed to reverse.

11. Defects

Like in bulk materials, defects in 2D materials can have a significant impact on their properties. In the next sections, we discuss the structure of defects and their effects on the properties of 2D materials. We classify the defects by their dimensionality into zero-dimensional point defects, one-dimensional line defects such as dislocations, grain boundaries, and edges, and two-dimensional area defects. For a discussion of experimental aspects of defects in 2D materials, we refer the reader to reviews on defects in 2D MoS$_2$, [278] graphene [279–281], and defect engineering in 2D materials [282].

11.1. Point defects

The same kind of point defects are possible in 2D and 3D systems: vacancies, interstitials, and substitutions or impurities. Naturally, these defects can also interact to form pairs or complexes. Because of the reduced dimensionality in 2D systems, point defects can dramatically affect the electronic conductivity, optical spectra, magnetic response, and other properties even at modest concentrations [278–282].

The most important quantity for point defects is their formation energy [283, 284]. The formation energy, $E_{\mathrm{def}}^{\mathrm{f}}$ for a defect, X, with charge q is given by

$$E_{\mathrm{def}}^{\mathrm{f}}[X^q] = E_{\mathrm{tot}}[X^q] - E_{\mathrm{tot}}[\mathrm{bulk}] \\ - \sum n_i \mu_i + q[\epsilon_{\mathrm{F}} + \epsilon_{\mathrm{v}}], \quad (5)$$

where $E_{\mathrm{tot}}[X^q]$ and $E_{\mathrm{tot}}[\mathrm{bulk}]$ are the total energies of the supercell containing the defect and perfect bulk structure, respectively, n_i and μ_i are the number and chemical potential, respectively, of the atomic species, i, comprising the defect. ϵ_{F} is the Fermi level with respect to the valence band maximum (VBM) and ϵ_{v} is the energy of the VBM of the pristine host. The formation energy of point defects determines their equilibrium concentration. Furthermore, equilibration of defects can be slow at ambient conditions. Hence, the defect concentration in 2D materials is a often controlled by synthesis conditions such as the local chemical potential of components and the Fermi level, e.g. set by the substrates.

Calculations of point defects require large simulation cells to approach the low concentration relevant for experiments

and to reduce the spurious interactions between the defect and its periodic images [285]. Convergence of the defect formation energy with simulation cell size works well for neutral defects, but special care has to be taken for charged defects.

Most DFT calculations employ plane-wave basis sets and periodic boundary conditions. To minimize the interactions between periodic images of the 2D materials in the direction perpendicular to the material, increasing amounts of vacuum spacing are added until the energy or other properties converge. For charged defects, the Poisson solver of plane-wave DFT codes implicitly assumes a compensating background charge and an average electrostatic potential of zero. However, unlike for bulk materials, 2D materials containing a net charge due to a charged defect display a linear divergence of the energy with vacuum spacing that is not corrected by a compensating uniform charge background. Furthermore, the electrostatic potential becomes quadratic in the vacuum region instead of linear, as would be the case for an isolated charged 2D material. As a consequence, the energy and forces are incorrect.

To correct this erroneous behavior requires either the addition of an energy correction, the modification of the compensating charge, or the truncation of the Coulomb interaction in the direction perpendicular to the 2D materials. Several energy correction schemes have been proposed, including corrections of the Madelung energy [286, 287] and the electrostatic potential. Reference [288] Richter *et al.* suggest a compensating charge that modifying the nuclear charge of one of the species in the charged material [289]. Alternative techniques that remove the spurious Coulomb interaction between periodic images of the 2D materials include Hockney's Fourier approximation to the Coulomb interaction [290] and improved reciprocal space method by Martyna and Tuckerman, [291] which, however, require large simulation cells. More recently, Genovese *et al.* developed an interpolating functions method that truncates the Coulomb interaction between periodic images of lower dimensional materials [292].

These computational methods provide potential solutions to the divergence issue for charged defects in 2D materials. However, the lack of implementation in widely available DFT codes still limits the number of calculations for charged defects in 2D materials. Furthermore, comparisons between the computational approaches and experimental validation are needed to determine the accuracy and efficiency of the various approaches for charged defects.

11.2. Line defects

Line defects in 2D materials are slightly different than in bulk materials. In 3D structures, a line defect and grain boundary are distinctly different, with the former being considered one-dimensional and the latter being two-dimensional. In 2D materials, line defects are equivalent to grain boundaries. There is no second direction for the structural defect to expand periodically, but these defects still define distinct grains within 2D materials. Thus, line defects and grain boundaries are treated as equivalent in the remainder of this review. We break the discussion into two sections: we first consider the structure of line defects, then discuss the properties that arise due to line defects.

11.2.1. Structure of line defects.

In the following, we discuss the structure of line defects in hexagonal planar and 2*H* structure monolayers. They are both hexagonal structures, and the dislocations are typically identified by the number of atoms that form a ring in the structure. For example, 4|8 is the notation used to denote a dislocation comprised of one four-atom ring and one eight-atom ring when viewed top down (see figure 21 (a)). A single dislocation does not constitute a line defect, but can be placed in series to construct a line defect. Thus, although dislocations are not themselves line defects in 2D materials, they are intrinsically linked to the discussion. To further clarify, line defects can either be continuous, i.e. able to continue indefinitely, or discontinuous with an eventual termination.

The hexagonal planar structure allows for several dislocations. These are primarily in the form of 5|7 and 5|5|8 defects in graphene, [294] though 5|9 dislocations have also been seen [295]. Grain boundaries composed of 4|8 dislocations have also been found to be stable in other planar hexagonal structures [296]. The dislocations that compose a grain boundary do not necessarily have to be periodic, as the boundary can be composed of a variety of dislocation types [297].

The 2*H* structure exists in AB_2 monolayers, the most common example being MoS_2 and other transition metal dichalcogenides. Zou *et al* predicted which dislocations can occur in MoS_2 and WS_2, and which can result in continuous line defects [293]. Of the dislocations predicted, a total of three retain stoichiometry in isolation: 4|8, and two forms of 5|7 (one with bridging metal atoms, one with bridging S atoms). S-rich defects include 6|8 and 5|7. Metal-rich include 4|6 and a 4|6 dislocation combined with two sulfur vacancies. These structures can be found in figure 21. In addition, bridging sulfur (8|8) and bridging molybdenum (5|5|8) dislocations have been computationally predicted to be stable and present in experimental MoS_2 [298]. 4|8, metal bridging 5|7 and S-rich 6|8 dislocations have also been verified experimentally [173, 299]. Finally, Zhou *et al* verified the existence of two 4|4 dislocations: one where two rings share a single sulfur atom at a point (4|4P) and the other where two rings share an edge of sulfur atoms (4|4E) [173].

11.2.2. Properties of line defects.

Self-doping is a prevalent phenomenon in graphene. The break in symmetry caused by line defects creates electronic states that act as n-type dopants [40]. This has been seen in extended 5|8|5 line defects, which also display ferromagnetic behavior [301, 302]. Other line defects composed of multiple dislocations have also been found to be magnetic [303].

In AB_2 (A = Mo, W; B = S, Se) monolayers, it is seen that 5|7 and 4|8 defects display magnetic behavior [300]. Both Mo- and S-rich 5|7 defects display ferromagnetic behavior (as seen in figure 22) while 4|8 defects are most stable when displaying antiferromagnetic order along the defect length. With regard to electronic structure, 4|4P defects have been predicted to act as a metallic strip in MoS_2 [173] while states within the band gap have been shown to arise in 4|8 defect loops [299].
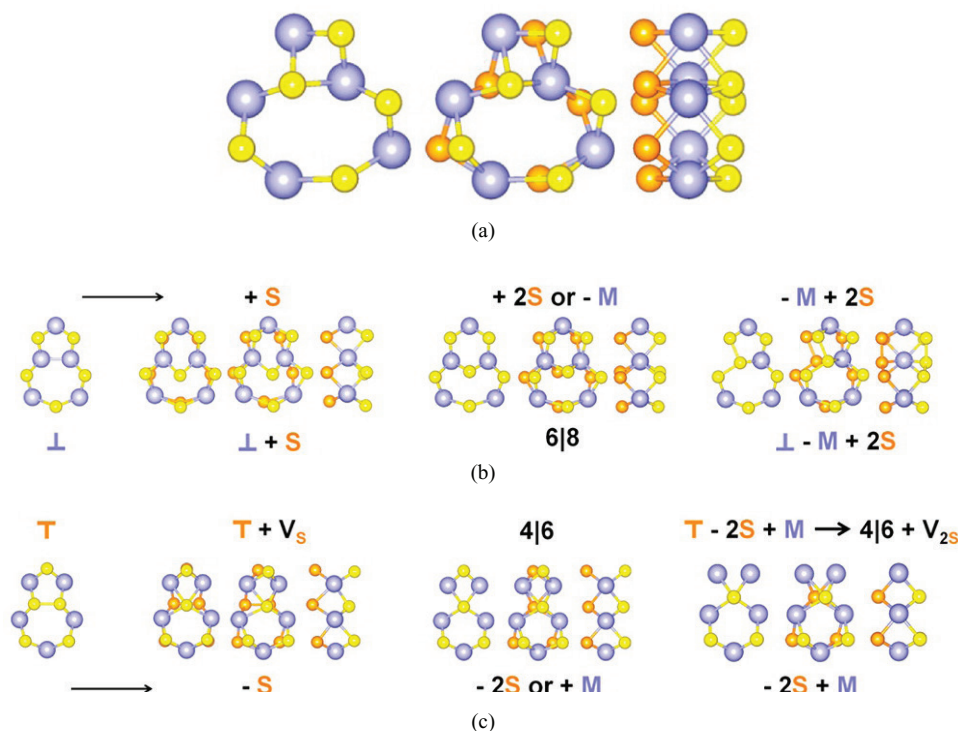
(a)

(b)

(c)

Figure 21. Dislocations in monolayer MoS_2. Each dislocation is shown from three perspectives: the top, slightly tilted, and side view of the monolayer (ordered from left to right). Dislocation (a) is referred to as 4|8. Dislocations (b) and (c) begin as 5|7 dislocations, then transition into different dislocations as atoms are added or removed. Reprinted (adapted) with permission from [293]. Copyright 2013 American Chemical Society.

11.3. Monolayer edges

Though monolayers are often modeled as if they continued indefinitely in two directions, experimental monolayers have edges. These edges have properties which are quite different from the 'bulk' of the monolayer, and have been investigated heavily as a route to tailor properties. In hexagonal and 2H structure monolayers, there are two basic edge terminations: zig-zag (ZZ) and armchair (AC), as seen in figure 23. For each of these edges, there can be varying atomic occupations for 2D materials with several layers of atoms (e.g. Mo-rich, S-rich). Edges are normally modeled in DFT calculations by creating a sufficiently wide nanoribbon.

Graphene displays magnetic moments in ZZ edges [304–306] but not AC edges [307–309]. The emergence of magnetism is due to the appearance of non-bonding π and π^* bands at the Fermi level, which significantly increases the density of states at the Fermi level [305, 307, 310]. The impact of these edge states on the bulk properties is found to decrease dramatically with ribbon thickness, indicating that this behavior is truly restricted to the ZZ edges [307, 308]. A break of symmetry that results in self doping is also present in the edges of graphene [40].

MoS_2 has been investigated to determine the shape of the unit cell under varying synthesis conditions. Using Wulff construction rules, Cao *et al* found that a Mo-rich environment results in a dodecagonal shape, S-rich in a triangular shape, and in between it takes varying hexagonal shapes [311]. The edges present are AC and three ZZ (S_2-rich, S-rich, Mo-rich), the latter two display magnetic behavior. The dodecagon
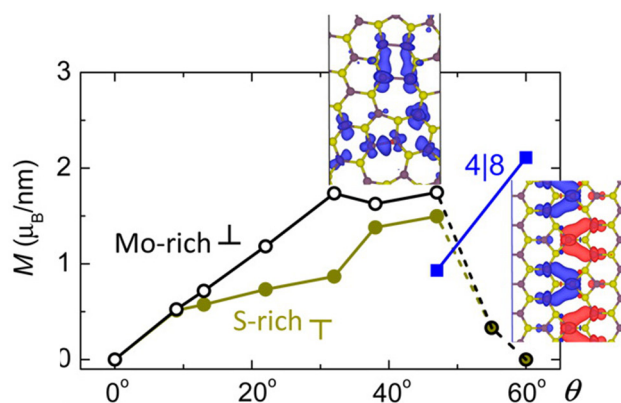

Figure 22. The amount of magnetization for the 5|7 and 4|8 defect loops in MoS_2, with regard to misorientation angle. All defects are assumed ferromagnetic in these calculations. One can see that Mo-rich defects are more magnetic than S-rich. Note that the 4|8 defect is found to display antiferromagnetic behavior in its most stable state. Reprinted with permission from [300]. Copyright 2013 American Chemical Society.

shape displays a significant amount of magnetism, but as the number of sides decreases (the synthesis environment becomes more S-rich) the magnetism disappears. In regard to electronic properties, the AC edge remains semiconducting while the ZZ edges exhibit metallic behavior. Reconstructions have also been observed in MoS_2. Though the reconstructions are found to be thermodynamically unstable, the lack of thermodynamic equilibrium during synthesis is thought to allow their existence [173].
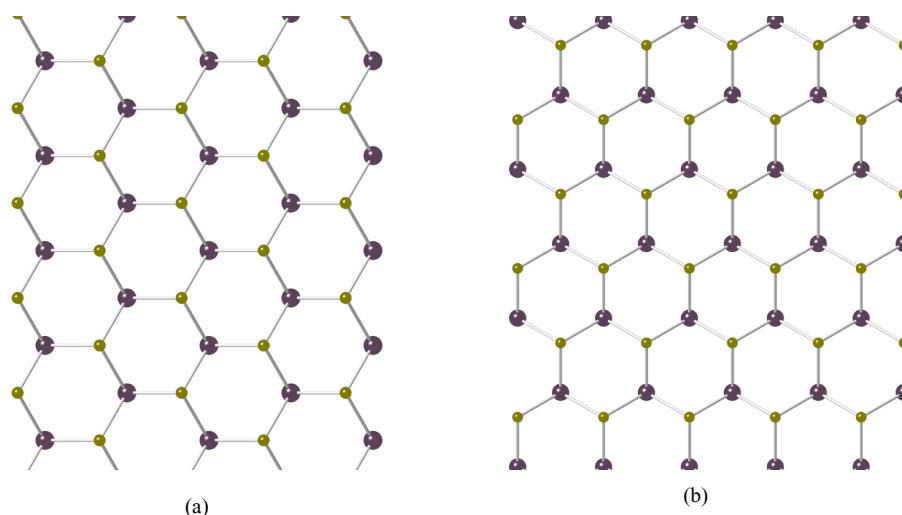
Figure 23. The two most common edge shapes of hexagonal and 2*H* monolayers. The (a) and (b) nanoribbons represent zigzag and armchair terminations, respectively.

11.4. Area defects

Area defects in 2D materials are primarily identified as Haeckelites. Haeckelites are extended regions of the dislocations discussed in section 11.2.1. These have been predicted computationally in 5|7 rings of graphene [312, 313] and in 4|8 rings of several TMDCs [314]. However, the authors of this review are not aware of these extended area defects appearing in the experimental literature.

12. Synthesis

12.1. Monolayer synthesis

Although the primary focus of this article is computation, it is important to know how 2D materials are synthesized. This section describes the available synthesis methods for 2D materials.

Broadly, there are three ways to obtain 2D materials: exfoliation, chemical vapor deposition (CVD), and etching. Exfoliation was the method used to synthesize graphene by Novoselov and Geim [1]. This method is suitable for synthesizing samples in a laboratory setting but difficult to extend to larger scales. CVD vaporizes species using heat and/or pressure, and releases them into a chamber with a cooled substrate. The vaporized species then deposit on the substrate, resulting in the self-assembly of a film. The crystallography of the film depends on the species in the air and on the substrate used. Finally, etching is used on materials such as the MAX phases, where sacrificial layers are removed by a solvent and monolayers are left suspended in solution.

12.2. Heterostructures

When building devices composed of monolayers, one can combine monolayers in a vertical or lateral heterostructure. The former is where the majority of research has been focused (and is discussed further in the next section), while lateral

heterostructures are more difficult to synthesize. However, it is an area of significant ongoing research interest [315–317]. Reviews specifically discussing monolayer heterostructures are available [318]. Both kinds of heterostructures are typically created by growing one monolayer at a time on a host substrate.

Lattice mismatch presents a challenge to the formation of both kinds of heterostructures. The importance of mismatch is somewhat lower for vertical heterostructures, as vdW bonding allows for a certain degree of incommensurability. Still, the alignment of the monolayers relative to each other can impact properties like conductivity if there are defects creating interfacial trap states. Lateral heterostructures are strained as a result of the strong covalent bonding at the junction boundary. In either case, mismatch can perturb or destroy the desired properties of the heterostructure. Charge transfer can also take place between the monolayers in a heterostructure and this can also cause otherwise unexpected behavior [319, 320].

13. Device simulation

Monolayer MoS_2 has attracted extensive research interest recently for its potential applications in nano-electronics, [321] flexible electronics, [322] and optoelectronics [323]. TMDC field-effect transistors (FETs) represent the ultimate thickness limit and exhibit superior immunity to short channel effects [324, 325]. The absence of thickness variation, surface roughness, and dangling bonds in these thin monolayer materials results in excellent intrinsic carrier transport properties and transistor scalability.

Furthermore, the mono- and few-layer TMDC materials are mechanically flexible and bendable. Thus, the materials and their heterojunctions have led to the development of numerous flexible electronic device designs [49]. Specific examples include low-power electronics for the switching circuitry of flexible displays and vertical steep sub-threshold device based electronics [326–329].

13.1. Approaches to device simulation

Carrier transport in semiconductor devices is traditionally modeled using semi-classical methods, such as the drift-diffusion theory for long channel silicon metal-oxide-semconductor field-effect transistors (MOSFETs). For nanoelectronic devices, quantum effects and atomistic-scale features inevitably become important. In response to this need, recent research has led to the evolution of a unified and powerful quantum transport simulation framework based on the non-equilibrium Green's function (NEGF) formalism [330–332].

It has been shown that the tunneling current is negligible in a device with 20 nm gate length, while direct source to drain tunneling is much more significant in a device with a gate length of 5 nm [333]. Hence, both the semi-classical and NEGF-based simulations have been applied to simulate 2D semiconductor devices. We focus on development and application of simulation approach and models to 2D devices. The studies on 2D semiconductor devices have been extensive and are beyond the scope of this review.

13.1.1. Semiclassical approach. Several semi-classical-based compact models of graphene, graphene nanoribbon, and bilayer graphene devices have been presented for digital and radio frequency applications and circuit design purpose [334–339]. Meanwhile, models based on a semi-classical approach for monolayer TMDC material and black phosphorous (BP) MOSFET have been developed for computational efficiency. A top-of-barrier model was used to study the performance limit of monolayer TMDC and BP based MOSFET [340, 341]. It showed that the device performance of monolayer TMDC and BP transistors outperform ultra-body-Si transistors with high-κ gate insulators, although the influence of scattering and contact resistance was not considered.

A drift-diffusion model was presented to study the I–V characteristics of a single TMDC long channel FET based on a lumped capacitance network [342]. An analytical model was used to study the subthreshold performance of a monolayer MoS$_2$ MOSFET [343]. The model consisted of three different subthreshold current sources, (1) subthreshold current, (2) band-to-band tunneling and (3) Shockley–Reed–Hall generation from the drain to body. A more rigorous model including all regions of MOSFET operation was derived for a 2D TMDC based MOSFET. [344] The model is also based on drift-diffusion theory but it also includes extrinsic effects such as interface traps, mobility degradation and inefficient source/drain doping. To facilitate circuit simulations, drift-diffusion-based compact models of lateral TMDC transistors have also been developed [345–347].

13.1.2. Quantum transport approach. As the channel length scales down to sub-20 nm range, quantum tunneling and quasi-ballistic transport effects can play a more important role in carrier transport. The non-equilibrium Green's function (NEGF) formalism, [330–332] which describes quantum effects, can be used to simulate quantum transport in nanodevices. Device performance of graphene and graphene nanoribbon-based nanoscale MOSFET and tunneling FET has been

thoroughly studied using the NEGF formalism [348–356]. In addition, ballistic NEGF transport simulations have been applied to study 2D TMDC and black phosphorous transistors with a channel length down to the sub-20 nm regime [357–367]. The effect of scattering can be treated in the NEGF formalism by using the self-consistent Born approximation.

Liu *et al* have shown that considering phonon scattering is important to accurately predict the performance of MoS$_2$ FETs [333]. They predict that an 8.1 nm long monolayer MoS$_2$ MOSFET can fulfill the ITRS requirements for high performance logic devices in 2023. Phonon scattering effects on monolayer WSe$_2$ n-type MOSFET and BP FET have also been investigated [368–370]. By using a double gate structure, it has been predicted that a bilayer MoS$_2$ FET can fulfill the requirement of HP devices up to a 6.6 nm gate length [370].

The effects of a doped contact and a metal contact on the performance of monolayer MoS$_2$ FET have been investigated by Han [367]. An Ohmic contact between semiconducting 2H MoS$_2$ and metallic 1T' MoS$_2$ has been demonstrated in a MoS$_2$ FET with a gate length of 7.5 nm [371]. Quantum transport simulations have been carried out and shown good subthreshold swing. Recently, a MoS$_2$ transistor with 1 nm gate length has demonstrated with subthreshold swing near the thermionic limit [372]. The performance of a MoS$_2$ FET with sub-5 nm gate length has also been studied [373]. The high frequency performance limit of a monolayer BP FET with a gate length of 10 nm has also been investigated [374]. In addition, the NEGF approach has been applied to study the performance of TMDC and BP tunneling FETs [364, 375–382].

13.2. In Silico device fabrication

Simulation cells for vertical heterostructures can be formed automatically using the MPInterfaces software package [116]. Based on the work of Zur and McGill [383], MPInterfaces will match two monolayers of arbitrary orientation in a single unit cell by minimizing both the cell size and the strain imposed on each layer. To the authors' knowledge, there are currently no open source tools available for the automatic construction of lateral heterostructures.

14. Outlook

Computational high-throughput methods have greatly accelerated the 2D materials discovery process as well as improved the in-depth understanding of their physical and chemical properties. Developing robust 2D databases will be crucial to expediting the spread of knowledge in the community. The application of advanced statistical analysis to these datasets remains an exciting and open frontier for discovering trends and physical rules for 2D materials.

Chemical substitutions are a simple way to expand the currently available 2D databases, and genetic algorithms can also be expected to contribute new stable 2D structures to these databases in the coming years. Developing machine learning models that interface to these methods would be one way to reduce the number of required objective function evaluations

(typically DFT calculations) and decrease the amount of time required to perform a thorough search.

As a result of their exciting potential, graphene and TMDCs have received the majority of focus in the areas of gaseous interactions and defect properties. However, we have listed many other classes of 2D materials that possess great potential for devices as well. High throughput tools to investigate the behavior of these monolayers when interacting with gases and exhibiting defects will streamline and improve these fields of research. In addition, the edge shapes of hexagonal and 2*H* monolayers are well-documented. New 2D structures, however, often do not exhibit the established 'zigzag' and 'armchair' terminations. Future work is expected regarding the edge terminations of these more exotic monolayer structures.

With growing computing power and improved theoretical methods, first-principles calculations of larger systems are becoming possible. This opens possibilities for discovering, e.g. new superconducting 2D materials and describing surfaces and interfaces more accurately. Modern experimental techniques, such as field effect doping, allow for modifying the electronic structure of covalently bonded thick layers, leading to rich prospects for new high T_c superconductors. Recent works show that first-principles electron–phonon calculations lead to meaningful results even in these often exotic electronic environments and can thus be an important tool to guide experimental understanding and fuel the discovery of novel superconductors.

2D materials hold promise for several applications. The recent discovery of monolayer half-metals and magnetic insulators has expanded the potential of ultra-thin spintronic devices. There has also been significant growth in the field of 2D materials that respond to stimuli, which could be used in a variety of devices. For many of these monolayers, whether they maintain their properties when assembled in heterostructures remains an open question. Much recent effort has focused on investigating the suitability of 2D materials to act as photocatalysts for hydrogen evolution, and this remains a particularly promising proposed application. There has been some research on carbon evolution, but overcoming the difficulties associated with the process is ongoing. Other potential redox reactions have yet to be investigated in as much detail, but they may enable routes to convert harmful liquids or gases into benign or useful byproducts.

The next several years of 2D materials research, supported by the onset of accessible 2D material databases, will undoubtedly produce many exciting results, and may see the emergence of 2D materials in commercial technologies.

Acknowledgment

ORCID iDs

R G Hennig ● https://orcid.org/0000-0003-4933-7686

References

[1] Novoselov K S, Geim A K, Morozov S V, Jiang D, Zhang Y, Dubonos S V, Grigorieva I V and Firsov A A 2004 *Science* **306** 666–9

[2] Mermin N D and Wagner H 1966 *Phys. Rev. Lett.* **17** 1133–6

[3] Le Doussal P and Radzihovsky L 1992 *Phys. Rev. Lett.* **69** 1209–12

[4] Nelson D, Piran T and Weinberg S 2004 *Statistical Mechanics of Membranes and Surfaces* (Singapore: World Scientific)

[5] Cassabois G, Valvin P and Gil B 2016 *Nat. Photon.* **10** 262–6

[6] Pacil D, Meyer J C, Girit C and Zettl A 2008 *Appl. Phys. Lett.* **92** 133107

[7] Splendiani A, Sun L, Zhang Y, Li T, Kim J, Chim C Y, Galli G and Wang F 2010 *Nano Lett.* **10** 1271–5

[8] Wang Q H, Kalantar-Zadeh K, Kis A, Coleman J N and Strano M S 2012 *Nat. Nanotechnol.* **7** 699–712

[9] Şahin H, Cahangirov S, Topsakal M, Bekaroglu E, Akturk E, Senger R T and Ciraci S 2009 *Phys. Rev. B* **80** 155453

[10] Ma R and Sasaki T 2010 *Adv. Mater.* **22** 5082–104

[11] Yin K, Zhang Y Y, Zhou Y, Sun L, Chisholm M F, Pantelides S T and Zhou W 2017 *2D Mater.* **4** 011001

[12] Naguib M, Mashtalir O, Carle J, Presser V, Lu J, Hultman L, Gogotsi Y and Barsoum M W 2012 *ACS Nano* **6** 1322–31

[13] Ashton M, Mathew K, Hennig R G and Sinnott S B 2016 *J. Phys. Chem. C* **120** 3550–6

[14] Zhuang H L and Hennig R G 2013 *Appl. Phys. Lett.* **103** 212102

[15] Zheng H, Li X B, Chen N K, Xie S Y, Tian W Q, Chen Y, Xia H, Zhang S B and Sun H B 2015 *Phys. Rev. B* **92** 115307

[16] Lebègue S and Eriksson O 2009 *Phys. Rev. B* **79** 115409

[17] Ashton M, Paul J, Sinnott S B and Hennig R G 2017 *Phys. Rev. Lett.* **118** 106101

[18] Zhou L, Kou L, Sun Y, Felser C, Hu F, Shan G, Smith S C, Yan B and Frauenheim T 2015 *Nano Lett.* **15** 7867–72

[19] Debbichi L, Kim H, Björkman T, Eriksson O and Lebègue S 2016 *Phys. Rev. B* **93** 245307

[20] Liu H, Neal A T, Zhu Z, Luo Z, Xu X, Tománek D and Ye P D 2014 *ACS Nano* **8** 4033–41

[21] Lebègue S, Björkman T, Klintenberg M, Nieminen R M and Eriksson O 2013 *Phys. Rev. X* **3** 031002

[22] Revard B C, Tipton W W, Yesypenko A and Hennig R G 2016 *Phys. Rev. B* **93** 054117

[23] Joensen P, Frindt R and Morrison S R 1986 *Mater. Res. Bull.* **21** 457–61

[24] Lin Y, Williams T V and Connell J W 2009 *J. Phys. Chem. Lett.* **1** 277–83

[25] Altuntasoglu O, Matsuda Y, Ida S and Matsumoto Y 2010 *Chem. Mater.* **22** 3158–64

[26] Coleman J N *et al* 2011 *Science* **331** 568–71

[27] Naguib M, Kurtoglu M, Presser V, Lu J, Niu J, Heon M, Hultman L, Gogotsi Y and Barsoum M W 2011 *Adv. Mater.* **23** 4248–53

[28] Lee Y H *et al* 2012 *Adv. Mater.* **24** 2320–5

[29] Cong C, Shang J, Wu X, Cao B, Peimyoo N, Qiu C, Sun L and Yu T 2014 *Adv. Opt. Mater.* **2** 131–6

[30] Li X, Magnuson C W, Venugopal A, Tromp R M, Hannon J B, Vogel E M, Colombo L and Ruoff R S 2011 *J. Am. Chem. Soc.* **133** 2816–9

[31] Hwang J *et al* 2012 *Acs Nano* **7** 385–95

[32] Zhuang H L and Hennig R G 2014 *JOM* **66** 366–74

[33] Singh A K, Zhuang H L and Hennig R G 2014 *Phys. Rev. B* **89** 245431

[34] Al Balushi Z Y *et al* 2016 *Nat. Mater.* **15** 1166–71

[35] Zhuang H L, Singh A K and Hennig R G 2013 *Phys. Rev. B* **87** 165415

[36] Zhuang H L, Johannes M D, Blonsky M N and Hennig R G 2014 *Appl. Phys. Lett.* **104** 022116

[37] Miro P, Audiffred M and Heine T 2014 *Chem. Soc. Rev.* **43** 6537–54

[38] Tang Q and Zhou Z 2013 *Prog. Mater. Sci.* **58** 1244–315

[39] Gupta A, Sakthivel T and Seal S 2015 *Prog. Mater. Sci.* **73** 44–126

[40] Castro Neto A H, Guinea F, Peres N M R, Novoselov K S and Geim A K 2009 *Rev. Mod. Phys.* **81** 109–62

[41] Shao Y, Wang J, Wu H, Liu J, Aksay I and Lin Y 2010 *Electroanalysis* **22** 1027–36

[42] Singh V, Joung D, Zhai L, Das S, Khondaker S I and Seal S 2011 *Prog. Mater. Sci.* **56** 1178–271

[43] Abergel D, Apalkov V, Berashevich J, Ziegler K and Chakraborty T 2010 *Adv. Phys.* **59** 261–482

[44] Lin Y and Connell J W 2012 *Nanoscale* **4** 6908–39

[45] Chhowalla M, Shin H S, Eda G, Li L J, Loh K P and Zhang H 2013 *Nat. Chem.* **5** 263–75

[46] Naguib M, Mochalin V N, Barsoum M W and Gogotsi Y 2014 *Adv. Mater.* **26** 992–1005

[47] Osada M and Sasaki T 2009 *J. Mater. Chem.* **19** 2503–11

[48] Khandelwal A, Mani K, Karigerasi M H and Lahiri I 2017 *Mater. Sci. Eng.* B **221** 17–34

[49] Geim A K and Grigorieva I V 2013 *Nature* **499** 419–25

[50] Niu T and Li A 2015 *Prog. Surf. Sci.* **90** 21–45 (special issue on silicene)

[51] Singh A K, Mathew K, Zhuang H L and Hennig R G 2015 *J. Phys. Chem. Lett.* **6** 1087–98

[52] Zhang T, Xue Q, Zhang S and Dong M 2012 *Nano Today* **7** 180–200

[53] Cockayne E, Mihalkovič M and Henley C L 2016 *Phys. Rev.* B **93** 020101

[54] Büchner C, Wang Z J, Burson K M, Willinger M G, Heyde M, Schlgl R and Freund H J 2016 *ACS Nano* **10** 7982–9

[55] IUCr Commission 1992 *Acta Crystallogr.* A **48** 922–46

[56] Mackay A L 1982 *Physica* A **114** 609–13

[57] Förster S, Meinel K, Hammer R, Trautmann M and Widdra W 2013 *Nature* **502** 215

[58] Huang P Y *et al* 2012 *Nano Lett.* **12** 1081–6

[59] Benedict L X, Chopra N G, Cohen M L, Zettl A, Louie S G and Crespi V H 1998 *Chem. Phys. Lett.* **286** 490–6

[60] Liu Z, Liu J Z, Cheng Y, Li Z, Wang L and Zheng Q 2012 *Phys. Rev.* B **85** 205418

[61] Qian X, Liu J, Fu L and Li J 2014 *Science* **346** 1344–7

[62] Zhuang H L, Johannes M, Singh A and Hennig R G 2017 *Phys. Rev.* B **96** 165305

[63] Zhu Z and Tománek D 2014 *Phys. Rev. Lett.* **112** 176802

[64] Guan J, Zhu Z and Tomanek D 2014 *ACS Nano* **8** 12763–8

[65] Wang G, Pandey R and Karna S P 2015 *ACS Appl. Mater. Interfaces* **7** 11490–6

[66] Sandoval E D, Hajinazar S and Kolmogorov A N 2016 *Phys. Rev.* B **94** 094105

[67] Zhao Y, Zeng S and Ni J 2016 *Phys. Rev.* B **93** 014502

[68] Li P and Luo W 2016 *Sci. Rep.* **6** 25423

[69] Matusalem F, Marques M, Teles L K and Bechstedt F 2015 *Phys. Rev.* B **92** 045436

[70] Singh A K, Revard B C, Ramanathan R, Ashton M, Tavazza F and Hennig R G 2017 *Phys. Rev.* B **95** 155426

[71] Ding Y, Wang Y, Ni J, Shi L, Shi S and Tang W 2011 *Phys. B: Condens. Matter* **406** 2254–60

[72] Thomas L H 1927 *Math. Proc. Camb. Phil. Soc.* **23** 542–8

[73] Fermi E 1927 *Rend. Accad. Naz. Lincei.* **6** 602–7

[74] Weizsäcker C F V 1935 *Z. Phys.* **96** 431–58

[75] Hohenberg P and Kohn W 1964 *Phys. Rev.* **136** B864–71

[76] Kohn W and Sham L J 1965 *Phys. Rev.* **140** A1133–8

[77] Vosko S H, Wilk L and Nusair M 1980 *Can. J. Phys.* **58** 1200–11

[78] Perdew J P and Zunger A 1981 *Phys. Rev.* B **23** 5048–79

[79] Perdew J P and Wang Y 1992 *Phys. Rev.* B **45** 13244–9

[80] Ceperley D M and Alder B J 1980 *Phys. Rev. Lett.* **45** 566–9

[81] Becke A D 2014 *J. Chem. Phys.* **140** 18A301

[82] Perdew J P, Burke K and Ernzerhof M 1996 *Phys. Rev. Lett.* **77** 3865–8

[83] Becke A D 1988 *Phys. Rev.* A **38** 3098–100

[84] Perdew J P *et al* 2017 *Proc. Natl Acad. Sci.* **114** 2801–6

[85] Perdew J P, Ernzerhof M and Burke K 1996 *J. Chem. Phys.* **105** 9982–5

[86] Heyd J, Scuseria G E and Ernzerhof M 2003 *J. Chem. Phys.* **118** 8207–15

[87] Batista E R, Heyd J, Hennig R G, Uberuaga B P, Martin R L, Scuseria G E, Umrigar C J and Wilkins J W 2006 *Phys. Rev.* B **74** 121102

[88] Parker W D, Wilkins J W and Hennig R G 2011 *Phys. Status Solidi* b **248** 267–74

[89] Hennig R G, Wadehra A, Driver K P, Parker W D, Umrigar C J and Wilkins J W 2010 *Phys. Rev.* B **82** 014101

[90] Anisimov V I, Zaanen J and Andersen O K 1991 *Phys. Rev.* B **44** 943–54

[91] Liechtenstein A I, Anisimov V I and Zaanen J 1995 *Phys. Rev.* B **52** R5467–70

[92] Dudarev S L, Botton G A, Savrasov S Y, Humphreys C J and Sutton A P 1998 *Phys. Rev.* B **57** 1505–9

[93] Hedin L 1965 *Phys. Rev.* **139** A796–823

[94] Aryasetiawan F and Gunnarsson O 1998 *Rep. Prog. Phys.* **61** 237

[95] Salpeter E E and Bethe H A 1951 *Phys. Rev.* **84** 1232–42

[96] Runge E and Gross E K U 1984 *Phys. Rev. Lett.* **52** 997–1000

[97] Yang Z H and Ullrich C A 2013 *Phys. Rev.* B **87** 195204

[98] Sharma S, Dewhurst J K, Sanna A and Gross E K U 2011 *Phys. Rev. Lett.* **107** 186401

[99] Grimme S 2006 *J. Comput. Chem.* **27** 1787–99

[100] Grimme S, Ehrlich S and Goerigk L 2011 *J. Comput. Chem.* **32** 1456–65

[101] Dion M, Rydberg H, Schröder E, Langreth D C and Lundqvist B I 2004 *Phys. Rev. Lett.* **92** 246401

[102] Klimeš J, Bowler D R and Michaelides A 2010 *J. Phys.: Condens. Matter* **22** 022201

[103] Tkatchenko A and Scheffler M 2009 *Phys. Rev. Lett.* **102** 073005

[104] Tkatchenko A, DiStasio R A, Car R and Scheffler M 2012 *Phys. Rev. Lett.* **108** 236402

[105] Björkman T, Gulans A, Krasheninnikov A V and Nieminen R M 2012 *Phys. Rev. Lett.* **108** 235502

[106] Zhou Y, Pellouchoud L A and Reed E J 2017 *2D Mater.* **4** 025005

[107] Pollack L and Perdew J P 2000 *J. Phys.: Condens. Matter* **12** 1239

[108] Kresse G and Hafner J 1993 *Phys. Rev.* B **47** 558–61

[109] Kresse G and Furthmüller J 1996 *Comput. Mater. Sci.* **6** 15–50

[110] Kresse G and Furthmüller J 1996 *Phys. Rev.* B **54** 11169–86

[111] Giannozzi P *et al* 2009 *J. Phys.: Condens. Matter* **21** 395502

[112] Gonze X *et al* 2009 *Comput. Phys. Commun.* **180** 2582–615 (40 YEARS OF CPC: a celebratory issue focused on quality software for high performance, grid and novel computing architectures)

[113] Milman V, Winkler B, White J A, Pickard C J, Payne M C, Akhmatskaya E V and Nobes R H 2000 *Int. J. Quantum Chem.* **77** 895–910

[114] Bahn S R and Jacobsen K W 2002 *Comput. Sci. Eng.* **4** 56–66

[115] Ong S P, Richards W D, Jain A, Hautier G, Kocher M, Cholia S, Gunter D, Chevrier V L, Persson K A and Ceder G 2013 *Comput. Mater. Sci.* **68** 314–9

[116] Mathew K, Singh A K, Gabriel J J, Choudhary K, Sinnott S B, Davydov A V, Tavazza F and Hennig R G 2016 *Comput. Mater. Sci.* **122** 183–90

[117] Rasmussen F A and Thygesen K S 2015 *J. Phys. Chem.* C **119** 13169–83

[118] Midwest nano infrastructure corridor 2D database http://apps.minic.umn.edu/2D/result.php (Accessed: 24 May 2017)

[119] Parlinski K, Li Z Q and Kawazoe Y 1997 *Phys. Rev. Lett.* **78** 4063–6

[120] Baroni S, de Gironcoli S, Dal Corso A and Giannozzi P 2001 *Rev. Mod. Phys.* **73** 515–62

[121] Togo A and Tanaka I 2015 *Scr. Mater.* **108** 1–5

[122] van de Walle A, Asta M D and Ceder G 2002 *Calphad* **26** 539–53

[123] van de Walle A 2009 *Calphad* **33** 266–78

[124] Lerch D, Wieckhorst O, Hart G L W, Forcade R W and Mller S 2009 *Modelling Simul. Mater. Sci. Eng.* **17** 055003

[125] Feng J, Hennig R G, Ashcroft N W and Hoffmann R 2008 *Nature* **451** 445–8

[126] Rudin S P, Jones M D and Albers R C 2004 *Phys. Rev.* B **69** 094117

[127] Jain A *et al* 2013 *APL Mater.* **1** 011002

[128] Ong S P, Wang L, Kang B and Ceder G 2008 *Chem. Mater.* **20** 1798–807

[129] Jain A, Hautier G, Ong S, Moore C, Fischer C, Persson K and Ceder G 2011 *Phys. Rev.* B **84** 045115

[130] Shulenburger L, Baczewski A, Zhu Z, Guan J and Tomnek D 2015 *Nano Lett.* **15** 8170–5

[131] Singh A K and Hennig R G 2014 *Appl. Phys. Lett.* **105** 042103

[132] Ashton M, Gabriel J, Matthew K, Sinnott S B and Hennig R G 2017 Materialsweb Database https://materialsweb.org

[133] Zhang C, Yin H, Han M, Dai Z, Pang H, Zheng Y, Lan Y Q, Bao J and Zhu J 2014 *ACS Nano* **8** 3761–70

[134] Persson K, Ekman M and Ozoliņš V 2000 *Phys. Rev.* B **61** 11221–4

[135] Hennig R G, Lenosky T J, Trinkle D R, Rudin S P and Wilkins J W 2008 *Phys. Rev.* B **78** 054121

[136] Souvatzis P, Eriksson O, Katsnelson M I and Rudin S P 2008 *Phys. Rev. Lett.* **100** 095901

[137] Kirkwood J G 1935 *J. Chem. Phys.* **3** 300–13

[138] Souvatzis P, Eriksson O, Katsnelson M and Rudin S 2009 *Comput. Mater. Sci.* **44** 888–94

[139] Belsky A, Hellenbrandt M, Karen V L and Luksch P 2002 *Acta Crystallogr.* B **58** 364–9

[140] Bahmann S and Kortus J 2013 *Comput. Phys. Commun.* **184** 1618–25

[141] Zhou X F, Dong X, Oganov A R, Zhu Q, Tian Y and Wang H T 2014 *Phys. Rev. Lett.* **112** 085502

[142] Zhou X F, Oganov A R, Wang Z, Popov I A, Boldyrev A I and Wang H T 2016 *Phys. Rev.* B **93** 085406

[143] Wang Z, Zhou X F, Zhang X, Zhu Q, Dong H, Zhao M and Oganov A R 2015 *Nano Lett.* **15** 6182–6

[144] Xiang H, Huang B, Li Z, Wei S H, Yang J and Gong X 2012 *Phys. Rev.* X **2** 011003

[145] Oganov A R and Glass C W 2006 *J. Chem. Phys.* **124** 244704

[146] Tipton W W and Hennig R G 2013 *J. Phys.: Condens. Matter* **25** 495401

[147] Revard B C, Tipton W W and Hennig R G 2014 *Structure and Stability Prediction of Compounds with Evolutionary Algorithms* (Cham: Springer)

[148] Wang Y, Lv J, Zhu L and Ma Y 2010 *Phys. Rev.* B **82** 094116

[149] Luo X, Yang J, Liu H, Wu X, Wang Y, Ma Y, Wei S H, Gong X and Xiang H 2011 *J. Am. Chem. Soc.* **133** 16285–90

[150] Wang Y, Miao M, Lv J, Zhu L, Yin K, Liu H and Ma Y 2012 *J. Chem. Phys.* **137** 224108

[151] Luo W, Ma Y, Gong X and Xiang H 2014 *J. Am. Chem. Soc.* **136** 15992–7

[152] Wu X, Dai J, Zhao Y, Zhuo Z, Yang J and Zeng X C 2012 *ACS Nano* **6** 7443–53

[153] Lu H, Mu Y, Bai H, Chen Q and Li S D 2013 *J. Chem. Phys.* **138** 024701

[154] Dai J, Zhao Y, Wu X, Yang J and Zeng X C 2013 *J. Phys. Chem. Lett.* **4** 561–7

[155] Zhang M, Gao G, Kutana A, Wang Y, Zou X, John S T, Yakobson B I, Li H, Liu H and Ma Y 2015 *Nanoscale* **7** 12023–9

[156] Ataca C, Sahin H and Ciraci S 2012 *J. Phys. Chem.* C **116** 8983–99

[157] Ashton M, Hennig R G, Broderick S R, Rajan K and Sinnott S B 2016 *Phys. Rev.* B **94** 054116

[158] Naguib M, Halim J, Lu J, Cook K M, Hultman L, Gogotsi Y and Barsoum M W 2013 *J. Am. Chem. Soc.* **135** 15966–9

[159] Mashtalir O, Naguib M, Mochalin V N, Dall'Agnese Y, Heon M, Barsoum M W and Gogotsi Y 2013 *Nat. Commun.* **4** 1716

[160] Ghidiu M, Naguib M, Shi C, Mashtalir O, Pan L, Zhang B, Yang J, Gogotsi Y, Billinge S and Barsoum M 2014 *Chem. Commun.* **50** 9517–20

[161] Khazaei M, Arai M, Sasaki T, Chung C Y, Venkataramanan N S, Estili M, Sakka Y and Kawazoe Y 2013 *Adv. Funct. Mater.* **23** 2185–92

[162] Urbankowski P, Anasori B, Makaryan T, Er D, Kota S, Walsh P L, Zhao M, Shenoy V B, Barsoum M W and Gogotsi Y 2016 *Nanoscale* **8** 11385–91

[163] Persson K A, Waldwick B, Lazic P and Ceder G 2012 *Phys. Rev.* B **85** 235438

[164] Mathew K, Sundararaman R, Letchworth-Weaver K, Arias T A and Hennig R G 2014 *J. Chem. Phys.* **140** 084106

[165] Leenaerts O, Partoens B and Peeters F M 2008 *Phys. Rev.* B **77** 125416

[166] Schedin F, Geim A K, Morozov S V, Hill E W, Blake P, Katsnelson M I and Novoselov K S 2007 *Nat. Mater.* **6** 652–5

[167] Fowler J D, Allen M J, Tung V C, Yang Y, Kaner R B and Weiller B H 2009 *ACS Nano* **3** 301–6

[168] Dan Y, Lu Y, Kybert N J, Luo Z and Johnson A T C 2009 *Nano Lett.* **9** 1472–5

[169] González B S, Hernández-Rojas J, Bretón J and Gomez Llorente J M 2007 *J. Phys. Chem.* C **111** 14862–9

[170] Zhang Y H, Chen Y B, Zhou K G, Liu C H, Zeng J, Zhang H L and Peng Y 2009 *Nanotechnology* **20** 185504

[171] Liu H, Han N and Zhao J 2015 *RSC Adv.* **5** 17572–81

[172] Qiu H *et al* 2013 *Nat. Commun.* **4** 2642

[173] Zhou W, Zou X, Najmaei S, Liu Z, Shi Y, Kong J, Lou J, Ajayan P M, Yakobson B I and Idrobo J C 2013 *Nano Lett.* **13** 2615–22

[174] Tongay S, Zhou J, Ataca C, Liu J, Kang J S, Matthews T S, You L, Li J, Grossman J C and Wu J 2013 *Nano Lett.* **13** 2831–6

[175] Tongay S *et al* 2013 *Sci. Rep.* **3** 2657

[176] Perdew J P and Levy M 1983 *Phys. Rev. Lett.* **51** 1884–7

[177] Perdew J P 1985 *Int. J. Quantum Chem.* **28** 497–523

[178] Zhuang H L and Hennig R G 2013 *Phys. Rev.* B **88** 115314

[179] Onida G, Reining L and Rubio A 2002 *Rev. Mod. Phys.* **74** 601–59

[180] Frenkel J 1931 *Phys. Rev.* **37** 17–44

[181] Wannier G H 1937 *Phys. Rev.* **52** 191–7

[182] Ross J S *et al* 2013 *Nat. Commun.* **4** 1474

[183] Mak K F, He K, Lee C, Lee G H, Hone J, Heinz T F and Shan J 2013 *Nat. Mater.* **12** 207–11

[184] Ziman J M 1979 *Principles of the Theory of Solids* (Cambridge: Cambridge University Press)

[185] Cheiwchanchamnangij T and Lambrecht W R L 2012 *Phys. Rev.* B **85** 205302

[186] Chow P K, Jacobs-Gedrim R B, Gao J, Lu T M, Yu B, Terrones H and Koratkar N 2015 *ACS Nano* **9** 1520–7

[187] Nair R R, Blake P, Grigorenko A N, Novoselov K S, Booth T J, Stauber T, Peres N M R and Geim A K 2008 *Science* **320** 1308–8

[188] Bernardi M, Palummo M and Grossman J C 2013 *Nano Lett.* **13** 3664–70

[189] Dumcenco D *et al* 2015 *ACS Nano* **9** 4611–20

[190] Tsai M L, Su S H, Chang J K, Tsai D S, Chen C H, Wu C I, Li L J, Chen L J and He J H 2014 *ACS Nano* **8** 8317–22

[191] Withers F *et al* 2015 *Nat. Mater.* **14** 301–6

[192] Kittel C 2005 *Introduction to Solid State Physics* 8th edn (New York: Wiley)

[193] Bak T, Nowotny J, Rekas M and Sorrell C 2002 *Int. J. Hydrog. Energy* **27** 991–1022

[194] Ni M, Leung M K, Leung D Y and Sumathy K 2007 *Renew. Sustain. Energy Rev.* **11** 401–25

[195] Sun Y *et al* 2012 *Angew. Chem. Int. Ed.* **51** 8727–31

[196] Sun Y *et al* 2012 *Nat. Commun.* **3** 1057

[197] Voiry D *et al* 2013 *Nat. Mater.* **12** 850–5

[198] Sun Y, Sun Z, Gao S, Cheng H, Liu Q, Lei F, Wei S and Xie Y 2014 *Adv. Energy Mater.* **4** 1614

[199] Xu Y, Zhao W, Xu R, Shi Y and Zhang B 2013 *Chem. Commun.* **49** 9803–5

[200] Liang L, Sun Y, Lei F, Gao S and Xie Y 2014 *J. Mater. Chem.* A **2** 10647–53

[201] Singh D, Gupta S K, Sonvane Y, Kumar A and Ahuja R 2016 *Catalysis Sci. Technol.* **6** 6605–14

[202] Gao J, Tay Q, Li P Z, Xiong W W, Zhao Y, Chen Z and Zhang Q 2014 *Chem. Asian J.* **9** 131–4

[203] Zhuang H L and Hennig R G 2013 *J. Phys. Chem.* C **117** 20440–5

[204] Zhuang H L and Hennig R G 2013 *Chem. Mater.* **25** 3232–8

[205] Chowdhury C, Karmakar S and Datta A 2017 *J. Phys. Chem.* C **121** 7615–24

[206] Wang J, Meng J, Li Q and Yang J 2016 *Phys. Chem. Chem. Phys.* **18** 17029–36

[207] Jiao Y, Zhou L, Ma F, Gao G, Kou L, Bell J, Sanvito S and Du A 2016 *ACS Appl. Mater. Interfaces* **8** 5385–92

[208] Liu J, Li X B, Wang D, Lau W M, Peng P and Liu L M 2014 *J. Chem. Phys.* **140** 054707

[209] Zhang X, Zhao X, Wu D, Jing Y and Zhou Z 2016 *Adv. Sci.* **3** 2198

[210] Liu J, Li X B, Wang D, Liu H, Peng P and Liu L M 2014 *J. Mater. Chem.* A **2** 6755–61

[211] Zhou L, Zhuo Z, Kou L, Du A and Tretiak S 2017 *Nano Lett.* **17** 4466–72

[212] Zhang X, Li B, Wang J, Yuan Y, Zhang Q, Gao Z, Liu L M and Chen L 2014 *Phys. Chem. Chem. Phys.* **16** 25854–61

[213] Wang J, Zhang M, Meng J, Li Q and Yang J 2017 *RSC Adv.* **7** 24446–52

[214] Guo Z, Zhou J, Zhu L and Sun Z 2016 *J. Mater. Chem.* A **4** 11446–52

[215] Ashton M, Sinnott S B and Hennig R G 2016 *Appl. Phys. Lett.* **109** 192103

[216] Ashton M, Gluhovic D, Sinnott S B, Guo J, Stewart D A and Hennig R G 2017 *Nano Lett.* **17** 5251–7

[217] Torun E, Sahin H, Singh S and Peeters F 2015 *Appl. Phys. Lett.* **106** 192404

[218] Wilkinson M, Cable J, Wollan E and Koehler W 1959 *Phys. Rev.* **113** 497

[219] Sivadas N, Daniels M W, Swendsen R H, Okamoto S and Xiao D 2015 *Phys. Rev.* B **91** 235425

[220] Kosterlitz J M and Thouless D J 1973 *J. Phys.* C: Solid State Phys. **6** 1181

[221] Šipr O, Bornemann S, Minár J, Polesya S, Popescu V, Šimnek A and Ebert H 2007 *J. Phys.: Condens. Matter.* **19** 096203

[222] Kan M, Adhikari S and Sun Q 2014 *Phys. Chem. Chem. Phys.* **16** 4990–4

[223] Zhang H, Dai Y M and Liu L M 2015 *Comput. Mater. Sci.* **101** 255–9

[224] Zhuang H L and Hennig R G 2016 *Phys. Rev.* B **93** 054429

[225] Chittari B L, Park Y, Lee D, Han M, MacDonald A H, Hwang E and Jung J 2016 *Phys. Rev.* B **94** 184428

[226] Zhuang H L, Xie Y, Kent P R C and Ganesh P 2015 *Phys. Rev.* B **92** 035407

[227] Li X and Yang J 2014 *J. Mater. Chem.* C **2** 7071–6

[228] Zhang S, Li Y, Zhao T and Wang Q 2014 *Sci. Rep.* **4** 5241

[229] Gong C *et al* 2017 *Nature* **546** 265–9

[230] Huang B *et al* 2017 *Nature* **546** 270–3

[231] Zhuang H L, Kent P R C and Hennig R G 2016 *Phys. Rev.* B **93** 134407

[232] Guo Y 2004 *Science* **306** 1915–7

[233] Sklyadneva I Y, Heid R, Bohnen K P, Echenique P M and Chulkov E V 2013 *Phys. Rev.* B **87** 085440

[234] Özer M M, Thompson J R and Weitering H H 2006 *Nat. Phys.* **2** 173–6

[235] Noffsinger J and Cohen M L 2010 *Phys. Rev.* B **81** 214519

[236] Zhang T *et al* 2010 *Nat. Phys.* **6** 104–8

[237] Noffsinger J and Cohen M L 2011 *Solid State Commun.* **151** 421–4

[238] Margine E R and Giustino F 2014 *Phys. Rev.* B **90** 014518

[239] Profeta G, Calandra M and Mauri F 2012 *Nat. Phys.* **8** 131–4

[240] Zheng J J and Margine E R 2016 *Phys. Rev.* B **94** 064509

[241] Einenkel M and Efetov K B 2011 *Phys. Rev.* B **84** 214508

[242] Ludbrook B M *et al* 2015 *Proc. Natl Acad. Sci.* **112** 11795–9

[243] Hsu F C *et al* 2008 *Proc. Natl Acad. Sci.* **105** 14262–4

[244] Wang Q Y *et al* 2012 *Chin. Phys. Lett.* **29** 037402

[245] Lee J J *et al* 2014 *Nature* **515** 245–8

[246] Hirschfeld P J 2016 *C. R. Phys.* **17** 197–231

[247] Li B, Xing Z W, Huang G Q and Xing D Y 2014 *J. Appl. Phys.* **115** 193907

[248] Wang Y, Linscheid A, Berlijn T and Johnston S 2016 *Phys. Rev.* B **93** 134513

[249] Singh D J and Du M H 2008 *Phys. Rev. Lett.* **100** 237003

[250] Zhou Y and Millis A J 2016 *Phys. Rev.* B **93** 224506

[251] Linscheid A 2016 *Supercond. Sci. Technol.* **29** 104005

[252] Maniadaki A E, Kopidakis G and Remediakis I N 2016 *Solid State Commun.* **227** 33–9

[253] Ni Z H, Yu T, Lu Y H, Wang Y Y, Feng Y P and Shen Z X 2008 *ACS Nano* **2** 2301–5

[254] Choi S M, Jhi S H and Son Y W 2010 *Phys. Rev.* B **81** 081407

[255] Mohr M, Papagelis K, Maultzsch J and Thomsen C 2009 *Phys. Rev.* B **80** 205410

[256] Wang J, Zhao R, Yang M, Liu Z and Liu Z 2013 *J. Chem. Phys.* **138** 084701

[257] Guzman D M and Strachan A 2014 *J. Appl. Phys.* **115** 243701

[258] Kou L, Frauenheim T and Chen C 2013 *J. Phys. Chem. Lett.* **4** 1730–6

[259] Guo H, Lu N, Wang L, Wu X and Zeng X C 2014 *J. Phys. Chem.* C **118** 7242–9

[260] Zhu Z, Guan J, Liu D and Tomnek D 2015 *ACS Nano* **9** 8284–90

[261] Zhang J and Meguid S A 2017 *Semicond. Sci. Technol.* **32** 043006

[262] Blonsky M N, Zhuang H L, Singh A K and Hennig R G 2015 *ACS Nano* **9** 9885–91

[263] Fei R, Li W, Li J and Yang L 2015 *Appl. Phys. Lett.* **107** 173104

[264] Li W and Li J 2015 *Nano Res.* **8** 3796–802

[265] Zeng Z, Tan C, Huang X, Bao S and Zhang H 2014 *Energy Environ. Sci.* **7** 797–803

[266] Lee C, Wei X, Kysar J W and Hone J 2008 *Science* **321** 385–8

[267] Mele E J and Král P 2002 *Phys. Rev. Lett.* **88** 056803

[268] Wang H and Qian X 2017 *2D Mater.* **4** 015042

[269] Baroni S, Giannozzi P and Testa A 1987 *Phys. Rev. Lett.* **58** 1861–4

[270] Gonze X 1995 *Phys. Rev.* A **52** 1086–95

[271] Gonze X 1995 *Phys. Rev.* A **52** 1096–114
[272] Wu X, Vanderbilt D and Hamann D R 2005 *Phys. Rev.* B **72** 035105
[273] Wang H, Zhang Y N, Wu R Q, Sun L Z, Xu D S and Zhang Z D 2013 *Sci. Rep.* **3** 3521
[274] Cullen J R 1995 *Phys. Rev.* B **52** 57–60
[275] Fei R, Faghaninia A, Soklaski R, Yan J A, Lo C and Yang L 2014 *Nano Lett.* **14** 6393–9
[276] Zhang G and Zhang Y W 2015 *Mech. Mater.* **91** 382–98
[277] Liu F *et al* 2016 *Nat. Commun.* **7** 12357
[278] Lin Z, Carvalho B R, Kahn E, Lv R, Rao R, Terrones H, Pimenta M A and Terrones M 2016 *2D Mater.* **3** 022002
[279] Terrones H, Lv R, Terrones M and Dresselhaus M S 2012 *Rep. Prog. Phys.* **75** 062501
[280] Yazyev O V and Chen Y P 2014 *Nat. Nano.* **9** 755–67
[281] Liu L, Qing M, Wang Y and Chen S 2015 *J. Mater. Sci. Technol.* **31** 599–606 (Special issue on 1D nanomaterials)
[282] Peng Q, Crean J, Dearden A K, Huang C, Wen X, Bordas S P and De S 2013 *Mod. Phys. Lett.* B **27** 1330017
[283] Van de Walle C G and Neugebauer J 2004 *J. Appl. Phys.* **95** 3851–79
[284] Zhang S and Northrup J E 1991 *Phys. Rev. Lett.* **67** 2339
[285] Cohen M L, Schlüter M, Chelikowsky J R and Louie S G 1975 *Phys. Rev.* B **12** 5575
[286] Rurali R, Palummo M and Cartoixà X 2010 *Phys. Rev.* B **81** 235304
[287] Komsa H P, Berseneva N, Krasheninnikov A V and Nieminen R M 2014 *Phys. Rev.* X **4** 031044
[288] Dabo I, Kozinsky B, Singh-Miller N E and Marzari N 2008 *Phys. Rev.* B **77** 115139
[289] Richter N A, Sicolo S, Levchenko S V, Sauer J and Scheffler M 2013 *Phys. Rev. Lett.* **111** 045502
[290] Hockney R W 1970 Potential calculation and some applications *Technical Report* Langley Research Center, Hampton, VA
[291] Martyna G J and Tuckerman M E 1999 *J. Chem. Phys.* **110** 2810–21
[292] Genovese L, Deutsch T, Neelov A, Goedecker S and Beylkin G 2006 *J. Chem. Phys.* **125** 074105
[293] Zou X, Liu Y and Yakobson B I 2013 *Nano Lett.* **13** 253–8
[294] Berger D and Ratsch C 2016 *Phys. Rev.* B **93** 235441
[295] Banhart F, Kotakoski J and Krasheninnikov A V 2011 *ACS Nano* **5** 26–41
[296] Camacho-Mojica D C and Lpez-Uras F 2016 *Chem. Phys. Lett.* **652** 73–8
[297] Huang P Y *et al* 2011 *Nature* **469** 389–92
[298] Enyashin A N, Bar-Sadan M, Houben L and Seifert G 2013 *J. Phys. Chem.* C **117** 10842–8
[299] van der Zande A M, Huang P Y, Chenet D A, Berkelbach T C, You Y, Lee G H, Heinz T F, Reichman D R, Muller D A and Hone J C 2013 *Nat. Mater.* **12** 554–61
[300] Zhang Z, Zou X, Crespi V H and Yakobson B I 2013 *ACS Nano* **7** 10475–81
[301] Ren J C, Ding Z, Zhang R Q and Van Hove M A 2015 *Phys. Rev.* B **91** 045425
[302] Kou L, Tang C, Guo W and Chen C 2011 *ACS Nano* **5** 1012–7
[303] Dutta S and Wakabayashi K 2015 *Sci. Rep.* **5** 11744
[304] Son Y W, Cohen M L and Louie S G 2006 *Nature* **444** 347–9
[305] Okada S and Oshiyama A 2001 *Phys. Rev. Lett.* **87** 146803
[306] Enoki T and Kobayashi Y 2005 *J. Mater. Chem.* **15** 3999–4002
[307] Fujita M, Wakabayashi K, Nakada K and Kusakabe K 1996 *J. Phys. Soc. Japan* **65** 1920–3
[308] Nakada K, Fujita M, Dresselhaus G and Dresselhaus M S 1996 *Phys. Rev.* B **54** 17954–61
[309] Kobayashi Y, Fukui K I, Enoki T, Kusakabe K and Kaburagi Y 2005 *Phys. Rev.* B **71** 193406
[310] Miyamoto Y, Nakada K and Fujita M 1999 *Phys. Rev.* B **59** 9858–61
[311] Cao D, Shen T, Liang P, Chen X and Shu H 2015 *J. Phys. Chem.* C **119** 4294–301
[312] Crespi V H, Benedict L X, Cohen M L and Louie S G 1996 *Phys. Rev.* B **53** R13303–5
[313] Terrones H, Terrones M, Hernández E, Grobert N, Charlier J C and Ajayan P M 2000 *Phys. Rev. Lett.* **84** 1716–9
[314] Terrones H and Terrones M 2014 *2D Mater.* **1** 011003
[315] Lee J, Huang J, Sumpter B G and Yoon M 2017 *2D Mater.* **4** 021016
[316] Zhang X Q, Lin C H, Tseng Y W, Huang K H and Lee Y H 2015 *Nano Lett.* **15** 410–5
[317] Son Y, Li M Y, Cheng C C, Wei K H, Liu P, Wang Q H, Li L J and Strano M S 2016 *Nano Lett.* **16** 3571–7
[318] Wang H, Liu F, Fu W, Fang Z, Zhou W and Liu Z 2014 *Nanoscale* **6** 12250–72
[319] Fang H *et al* 2014 *Proc. Natl Acad. Sci.* **111** 6198–202
[320] Novoselov K S, Mishchenko A, Carvalho A and Castro Neto A H 2016 *Science* **353** aac9439
[321] Fiori G, Bonaccorso F, Iannaccone G, Palacios T, Neumaier D, Seabaugh A, Banerjee S K and Colombo L 2014 *Nat. Nanotechnol.* **9** 768–79
[322] Akinwande D, Petrone N and Hone J 2014 *Nat. Commun.* **5** 5678
[323] Xia F, Wang H, Xiao D, Dubey M and Ramasubramaniam A 2014 *Nat. Photon.* **8** 899–907
[324] Liu H, Neal A T and Ye P D 2012 *ACS Nano* **6** 8563–9
[325] Roy T, Tosun M, Kang J S, Sachid A B, Desai S B, Hettick M, Hu C C and Javey A 2014 *ACS Nano* **8** 6259–64
[326] Yu W J, Li Z, Zhou H, Chen Y, Wang Y, Huang Y and Duan X 2013 *Nat. Mater.* **12** 246–52
[327] Lee C H *et al* 2014 *Nat Nano* **9** 676–81
[328] Wang H *et al* 2012 Large-scale 2D electronics based on single-layer MoS₂ grown by chemical vapor deposition *Int. Electron Devices Meeting* pp 4.6.1–4
[329] Wang H, Yu L, Lee Y H, Shi Y, Hsu A, Chin M L, Li L J, Dubey M, Kong J and Palacios T 2012 *Nano Lett.* **12** 4674–80
[330] Keldysh L V 1965 *Sov. Phys.—JETP* **20** 1018
[331] Datta S 1997 *Quantum Transport* (Cambridge: Cambridge University Press)
[332] Ferry D K and Goodnick S M 1997 *Transport in Nanostructures* (Cambridge: Cambridge University Press)
[333] Liu L, Lu Y and Guo J 2013 *IEEE Trans. Electron Devices* **60** 4133–9
[334] Wang H, Hsu A, Kong J, Antoniadis D A and Palacios T 2011 *IEEE Trans. Electron Devices* **58** 1523–33
[335] Jimenez D 2011 *IEEE Trans. Electron Devices* **58** 4377–83
[336] Thiele S and Schwierz F 2011 *J. Appl. Phys.* **110** 034506
[337] Frégonése S, Magallo M, Maneux C, Happy H and Zimmer T 2013 *IEEE Trans. Nanotechnol.* **12** 539–46
[338] Cheli M, Fiori G and Iannaccone G 2009 *IEEE Trans. Electron Devices* **56** 2979–86
[339] Fahad M S, Srivastava A, Sharma A K and Mayberry C 2016 *IEEE Trans. Nanotechnol.* **15** 39–50
[340] Liu L, Kumar S B, Ouyang Y and Guo J 2011 *IEEE Trans. Electron Devices* **58** 3042–7
[341] Lam K T, Dong Z and Guo J 2014 *IEEE Electron Device Lett.* **35** 963–5
[342] Jimnez D 2012 *Appl. Phys. Lett.* **101** 243501
[343] Kshirsagar C, Xu W, Kim C H and Koester S J 2014 Design and analysis of MoS₂-based mosfets for ultra-low-leakage

dynamic memory applications *72nd Device Research Conf.* pp 187–8

[344] Cao W, Kang J, Liu W and Banerjee K 2014 *IEEE Trans. Electron Devices* **61** 4282–90

[345] Suryavanshi S V and Pop E 2015 Physics-based compact model for circuit simulations of 2D semiconductor devices *73rd Annual Device Research Conf.* pp 235–6

[346] Yadav C, Agarwal A and Chauhan Y S 2017 *IEEE Trans. Electron Devices* **64** 1261–8

[347] Jiang C, Liang R, Wang J and Xu J 2015 *AIP Adv.* **5** 057122

[348] Chauhan J, Liu L, Lu Y and Guo J 2012 *J. Appl. Phys.* **111** 094313

[349] Ouyang Y, Campbell P and Guo J 2008 *Appl. Phys. Lett.* **92** 063120

[350] Chauhan J and Guo J 2011 *Nano Res.* **4** 571–9

[351] Yoon Y and Guo J 2007 *Appl. Phys. Lett.* **91** 073103

[352] Ouyang Y, Yoon Y and Guo J 2007 *IEEE Trans. Electron Devices* **54** 2223–31

[353] Ouyang Y, Wang X, Dai H and Guo J 2008 *Appl. Phys. Lett.* **92** 243124

[354] Yoon Y, Fiori G, Hong S, Iannaccone G and Guo J 2008 *IEEE Trans. Electron Devices* **55** 2314–23

[355] Zhao P, Chauhan J and Guo J 2009 *Nano Lett.* **9** 684–8

[356] Ouyang Y, Dai H and Guo J 2010 *Nano Res.* **3** 8–15

[357] Yoon Y, Ganapathi K and Salahuddin S 2011 *Nano Lett.* **11** 3768–73

[358] Alam K and Lake R K 2012 *IEEE Trans. Electron Devices* **59** 3250–4

[359] Mishra V, Smith S, Ganapathi K and Salahuddin S 2013 Dependence of intrinsic performance of transition metal dichalcogenide transistors on materials and number of layers at the 5 nm channel-length limit *IEEE Int. Electron Devices Meeting* **5** 1–4

[360] Liu F, Wang Y, Liu X, Wang J and Guo H 2014 *IEEE Trans. Electron Devices* **61** 3871–6

[361] Wan R, Cao X and Guo J 2014 *Appl. Phys. Lett.* **105** 163511

[362] Cao X and Guo J 2015 *IEEE Trans. Electron Devices* **62** 659–65

[363] Yin D, Han G and Yoon Y 2015 *IEEE Electron Device Lett.* **36** 978–80

[364] Yin D and Yoon Y 2016 *J. Appl. Phys.* **119** 214312

[365] Banerjee L, Mukhopadhyay A, Sengupta A and Rahaman H 2016 *J. Comput. Electron.* **15** 919–30

[366] Luo S, Lam K T, Wang B, Hsu C H, Huang W, Yao L Z, Bansil A, Lin H and Liang G 2017 *IEEE Trans. Electron Devices* **64** 579–86

[367] Han G and Yoon Y 2014 *Appl. Phys. Lett.* **105** 213508

[368] Sengupta A, Chanana A and Mahapatra S 2015 *AIP Adv.* **5** 027101

[369] Lam K T, Luo S, Wang B, Hsu C H, Bansil A, Lin H and Liang G 2015 Effects of interlayer interaction in van der Waals layered black phosphorus for sub-10 nm FET *IEEE Int. Electron Devices Meeting* pp 12.2.1–4

[370] Cao W, Kang J, Sarkar D, Liu W and Banerjee K 2015 *IEEE Trans. Electron Devices* **62** 3459–69

[371] Nourbakhsh A *et al* 2016 *Nano Lett.* **16** 7798–806

[372] Desai S B *et al* 2016 *Science* **354** 99–102

[373] Dong Z and Guo J 2017 *IEEE Trans. Electron Devices* **64** 622–8

[374] Yin D, AlMutairi A and Yoon Y 2017 *IEEE Trans. Electron Devices* **64** 2984–21

[375] Lam K T, Cao X and Guo J 2013 *IEEE Electron Device Lett.* **34** 1331–3

[376] Ghosh R K and Mahapatra S 2013 *IEEE J. Electron Devices Soc.* **1** 175–80

[377] Lam K T, Seol G and Guo J 2014 Performance evaluation of MoS$_2$-WTe$_2$ vertical tunneling transistor using real-space quantum simulator *IEEE Int. Electron Devices Meeting* **30** 1–4

[378] Chang J and Hobbs C 2015 *Appl. Phys. Lett.* **106** 083509

[379] Liu F, Shi Q, Wang J and Guo H 2015 *Appl. Phys. Lett.* **107** 203501

[380] Agarwal T, Radu I, Raghavan P, Fiori G, Thean A, Heyns M and Dehaene W 2016 Effect of material parameters on two-dimensional materials based TFETs: an energy-delay perspective *46th European Solid-State Device Research Conf.* pp 47–50

[381] Ilatikhameneh H, Tan Y, Novakovic B, Klimeck G, Rahman R and Appenzeller J 2015 *IEEE J. Exploratory Solid-State Comput. Devices Circuits* **1** 12–8

[382] Chen F, Ilatikhameneh H, Tan Y, Valencia D, Klimeck G and Rahman R 2017 *J. Phys.: Conf. Ser.* **864** 012053

[383] Zur A and McGill T C 1984 *J. Appl. Phys.* **55** 378–86